International Journal of Fatigue 214 (2027) 109883

Contents lists available at ScienceDirect

International Journal of Fatigue

journal homepage: www.elsevier.com/locate/ijfatigue

Stable deformation growth as a fatigue life indicator for concrete: Experimental and multiscale numerical insights

Wassim Kerkeni [a], Abedulgader Baktheer [b], Mario Aguilar [a,*], Henrik Becks [c], Miroslav Vořechovský [d], Martin Classen [c], Rostislav Chudoba [a]

[a] Center for Structural Concrete Physics, RWTH Aachen University, Im Süsterfeld 9, 52072 Aachen, Germany
[b] Institute of Mechanics and Computational Mechanics, Leibniz Universität Hannover, 30167 Hannover, Germany
[c] Institute of Structural Concrete, RWTH Aachen University, Mies-van-der-Rohe-Straße 1, 52074 Aachen, Germany
[d] Institute of Structural Mechanics, Brno University of Technology, Veveří 95, 602 00 Brno, Czech Republic

ARTICLE INFO

Keywords:
Fatigue fracture
Concrete
S–N curves
Experimental investigations
Microplane model
Lattice discrete particle model
Lifetime prediction

ABSTRACT

Ensuring structural safety and durability requires accurate fatigue life prediction. Currently, the S–N (Wöhler) curves are well-established for evaluating the fatigue life of concrete, yet the obtained results in experimental investigations regularly reveal notable scatter. Recent studies point toward an alternative fatigue life assessment approach, which is referred to as the Sparks–Menzies relation and provides a strain-based failure criterion based on a linear relationship between the logarithmic strain rate in the second fatigue phase and the logarithmic number of cycles to failure. While previous research primarily focuses on the compressive fatigue behavior observed through cylinder tests, this study additionally applies the Sparks–Menzies relation to assess tensile fatigue life using notched three-point bending tests (3PBT) and shear fatigue life using punch-through shear tests (PTST), while also considering a broad range of varied test parameters. The experimental analysis validates the Sparks–Menzies relation as a highly reliable approach for fatigue life assessment, yielding coefficients of determination between R^2 = 0.954 and 0.998, whereas the corresponding S–N regressions ranged from R^2 = 0.329 to 0.907 and, in some cases, no meaningful linear regression could be established due to the pronounced scatter. Furthermore, the predictive capability of the strain-based evaluation approach has the potential to enable the estimation of the remaining fatigue life of runout specimens. In addition to the experimental investigation, meso- and macro-scale numerical simulations are performed to examine whether the linear relationship underlying the Sparks–Menzies relation can also be reproduced by physically motivated fatigue models. The simulations are based on a recently proposed fatigue hypothesis, in which fatigue degradation in concrete is driven by the cumulative inelastic sliding within inter-aggregate regions. To this end, a microplane constitutive model and a lattice discrete model developed by the authors are employed. Both models successfully reproduce the experimentally observed linear correlation between the logarithmic strain rate in the secondary fatigue phase and the logarithmic number of cycles to failure, thereby providing independent numerical confirmation of the Sparks–Menzies relation and supporting the underlying fatigue mechanism.

1. Introduction

Reliable prediction of structural lifetime plays a crucial role in ensuring safety and durability under high-cycle loading. Specifically, bridges and wind turbine towers are exposed to millions of loading cycles as a consequence of their slender cross sections, ultimately resulting in growing demand for new constructions in the coming decades [1–6]. Current research focuses on the implementation of various monitoring concepts designed to continuously measure the strain development of existing structures (Fig. 1a), and therefore establish the framework for accurate remaining service life predictions [7–12]. Following this development, consistent fatigue life assessment methods are required to effectively utilize and evaluate future monitoring data. Despite exhibiting considerable scatter within experimental investigations, the S–N curves [13–18] are currently well established for characterizing the fatigue life of concrete. However, the degradation process during the fatigue life is not captured in the strength-based S–N diagram, preventing essential integration into the advancing monitoring concepts. In general, the fatigue degradation process is described as

* Corresponding author.
E-mail address: maguilar@imb.rwth-aachen.de (M. Aguilar).

https://doi.org/10.1016/j.ijfatigue.2026.109883
Received 4 June 2026; Received in revised form 11 July 2026; Accepted 15 July 2026
Available online 1 August 2026
0142-1123/© 2026 The Authors. Published by Elsevier Ltd. This is an open access article under the CC BY license (http://creativecommons.org/licenses/by/4.0/).

Nomenclature

Abbreviations

3PBT	Three point bending test
CTOD	Crack tip opening displacement
H–L	High–low scenario
L–H	Low–high scenario
LDPM	Lattice discrete particle model
LVDT	Linear variable differential transformer
PTST	Punch-through-shear tests

Symbols

$\beta_{\mathrm{N}}^{\mathrm{mic}}$	Normal microplane integrity parameter
$\beta_{\mathrm{T}}^{\mathrm{mic}}$	Tangential microplane integrity parameter
$\boldsymbol{\alpha}_{\mathrm{T}}$	Kinematic hardening state variable
$\boldsymbol{\sigma}_{\mathrm{N}}^{\mathrm{P}}$	Normal plastic stress
$\boldsymbol{\sigma}_{\mathrm{T}}^{\mathrm{P}}$	Tangential plastic stress vector
$\boldsymbol{\theta}$	Rotation vector
$\boldsymbol{\varepsilon}$	Macroscopic strain tensor
$\boldsymbol{n}_{\mathrm{N}}$	Facet normal vector
$\boldsymbol{n}_{\mathrm{T}}$	Facet tangential vector
$\boldsymbol{u}$	Displacement vector
$\boldsymbol{u}^{\mathrm{P}}$	Plastic displacement vector
$\boldsymbol{x}$	Position vector
$\boldsymbol{X}_{\mathrm{T}}$	Back stress vector
$\boldsymbol{f}$	Force vector
$\boldsymbol{m}$	Moment vector
$\boldsymbol{\beta}$	Fourth-order damage inverse/integrity tensor
$\boldsymbol{\mathcal{E}}$	State variables vector
$\boldsymbol{S}$	Thermodynamic forces vector
$\boldsymbol{\sigma}$	Macroscopic stress tensor
$\boldsymbol{\varepsilon}_{\mathbf{T}}$	Tangential microplane strain vector
$\boldsymbol{\varepsilon}^{\mathrm{P}}$	Macroscopic plastic strain tensor
$\boldsymbol{C}^{\mathrm{e}}$	Fourth-order elastic stiffness tensor
$\boldsymbol{N}$	Second-order normal projection tensor
$\boldsymbol{T}$	Third-order tangential projection tensor
$\Delta\varepsilon_{\mathrm{II}}^{\max}$	Strain growth in the second fatigue phase
ΔN	Increment of load cycles
γ_{T}	Kinematic hardening modulus
ω_{N}	Normal damage state variable
$\omega_{\mathrm{N}}^{\mathrm{mic}}$	Normal microplane damage parameter
ω_{T}	Tangential damage state variable
$\omega_{\mathrm{T}}^{\mathrm{mic}}$	Tangential microplane damage parameter
ψ	Helmholtz free energy function
ρ	Material density
$\sigma_{\mathrm{c,mean}}$	Lateral compressive stress in PTST specimen
$\varepsilon^{\max}$	Strain at upper loading level
$\varepsilon_{N}^{\mathrm{P,mic}}$	Normal microplane plastic strain
$\varepsilon_{Tr}^{\mathrm{P,mic}}$	Tangential microplane plastic strain
ε_{N}	Normal microplane strain
E_{N}	Normal elastic modulus
E_{T}	Tangential elastic modulus
F	Applied external force
K_{T}	Isotropic hardening modulus
m, s	Parameters of Sparks–Menzies relation
N	Loading cycle
N_{f}	Cycles to failure
p_{T}	Pressure sensitivity parameter
$S_{\max}$	Upper bound of fatigue loading
$S_{\min}$	Lower bound of fatigue loading
Y_{N}	Normal energy release rate
Y_{T}	Tangential energy release rate
Z_{T}	Isotropic hardening stress
z_{T}	Isotropic hardening variable

a function of measured strain and applied loading cycles [19–23]. This function, denoted as fatigue creep curve hereinafter, is qualitatively depicted in Fig. 1b, illustrating the characteristic three-phase strain development of concrete subjected to fatigue loading. Initially, a rapid strain increase is observed up to 20% of the lifetime, followed by the second phase exhibiting linear strain growth up to 80% of consumed life and finally the third phase marked by accelerated strain progression, eventually leading to failure. In 1973, Sparks and Menzies [24] reported a linear correlation between the number of cycles to failure N_f and the slope of the strain growth during the second fatigue phase, i.e., the secondary strain rate $\varepsilon'_{\mathrm{II}} = \Delta\varepsilon_{\mathrm{II}}^{\max}/\Delta N$, on a double logarithmic scale. This relationship, qualitatively illustrated in Fig. 1c and defined as

$$\log \varepsilon'_{\mathrm{II}} = \log\left(\frac{\Delta\varepsilon_{\mathrm{II}}^{\max}}{\Delta N}\right) \approx m + s \log N_{\mathrm{f}}, \tag{1}$$

provides a strain-based approach for accurate fatigue life assessment and could thus be incorporated into monitoring concepts. Recent studies evaluating the validity of the Sparks–Menzies relation have predominantly concentrated on the compressive fatigue behavior of concrete [25–31], revealing that the linear correlation is independent of fiber content [32] as well as specimen size [33] and thus appears to depend solely on the concrete matrix. However, to allow for well-founded conclusions, additional experimental validation considering a broader range of test setups and loading configurations is of vital importance.

Although the Sparks–Menzies relation has been repeatedly observed experimentally, its physical origin and its connection to the underlying fatigue degradation mechanisms remain insufficiently understood. In this context, physically motivated numerical models provide an essential tool to examine whether the experimentally observed linear relationship between secondary deformation growth and fatigue life emerges naturally from the governing mechanisms of crack evolution, stress redistribution, and damage accumulation in concrete.

In tension, cohesive zone models are widely applied to simulate crack initiation and growth under cyclic and mixed-mode loading [34–38]. Their strength lies in capturing discrete cracking processes, while microplane formulations have further highlighted the role of triaxial stress redistribution in the fracture process zone [39–41]. Phenomenological damage–plasticity models remain the most common approach [42–45]. These frameworks efficiently reproduce macroscopic trends such as S–N curves and fatigue creep [46,47], but often neglect that compressive fatigue is governed by diffuse microcracking and local stress redistribution. More advanced formulations, such as the microplane model MS1 [48], incorporate these effects, though continuum models inevitably average out mesostructural features like aggregate interlock and crack interactions. Mesoscale models address this limitation by explicitly resolving concrete heterogeneity. By capturing crack evolution, stress transfer, and damage accumulation at the aggregate scale, they provide deeper mechanistic insights and often yield more reliable fatigue life predictions under complex loading [49–51].

This paper builds upon a series of experimental and numerical investigations previously conducted by the authors to comprehensively evaluate the applicability of the Sparks–Menzies relation for concrete

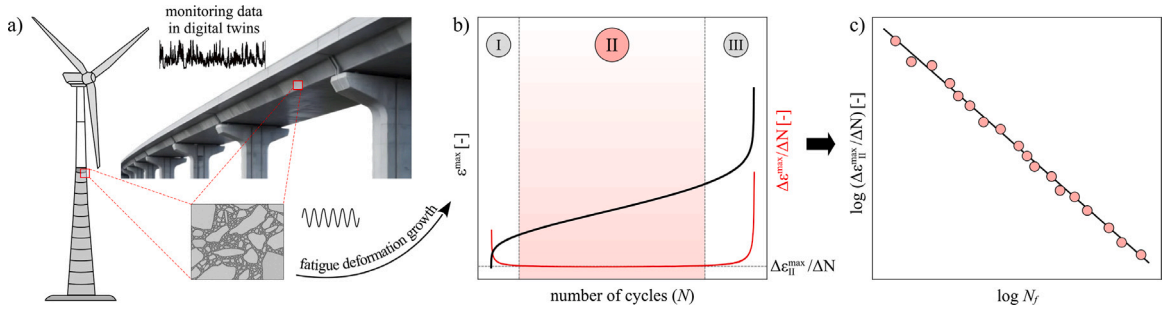


Fig. 1. (a) Motivation for applying the Sparks–Menzies relation to fatigue-loaded structures, highlighting deformation growth and its potential integration into data-driven digital twin frameworks; (b) Fatigue creep curve and strain rate–cycles relationship, showing linear secondary deformation as the basis for the Sparks–Menzies relation; (c) Simplified illustration of the Sparks–Menzies relation.

fatigue. In addition to compressive fatigue tests on cylindrical specimens, the study incorporates tensile fatigue tests on notched three-point bending specimens and shear fatigue tests using the punch-through shear setup. For all configurations, fatigue life is consistently evaluated using both the Sparks–Menzies relation and the conventional S–N approach, allowing for a direct and systematic comparison between the two assessment methods.

This study offers a novel and comprehensive examination of the validity and generality of the Sparks–Menzies relation across a wide range of stress states and experimental configurations, supported by complementary numerical analyses at multiple scales. Specifically, the paper extends the assessment to numerical simulations of uniaxial compressive fatigue using the microplane model MS1 and the lattice discrete particle model (LDPM), thereby linking macroscopic observations with micromechanical insights. The overall objective is to establish a unified understanding of the fatigue behavior of concrete under diverse loading conditions and to evaluate the applicability and robustness of the Sparks–Menzies relation as a strain-based fatigue life assessment criterion.

2. Evaluation of experimental data on concrete fatigue

The analysis of experimental results covers a wide range of loading conditions and test configurations. In addition to compressive fatigue tests on cylindrical concrete specimens, the applicability of the Sparks–Menzies relation is evaluated for tensile fatigue using notched three-point bending tests (3PBT) and for shear fatigue using punch-through shear tests (PTST), as summarized in Fig. 2. For all investigated test series, the fatigue life is additionally assessed using the classical S–N approach, enabling a systematic comparison between deformation-based and stress-based fatigue life evaluation methods.

2.1. Compressive cylinder tests with varied loading frequencies

The first experimental series is part of the study presented in [52] and investigates the influence of loading frequency on compressive fatigue behavior. In accordance with the fib Model Code 2010 [53], the concrete used in this test series is classified as concrete strength class C40. The cylinder test specimens measured 150 mm in diameter and 300 mm in height as shown in Fig. 3. The concrete was produced using CEM I 52.5 R cement with a water-to-cement ratio of 0.633 and quartz aggregate with a maximum grain size of 8 mm. To continuously monitor the strain development throughout the performed fatigue tests, three linear variable differential transformers (LVDTs) were attached around the cylinders at 120-degree intervals. The constant-amplitude fatigue loading was applied with frequencies of 2 Hz, 8.5 Hz and 55 Hz. The upper load levels ranged from $S_{max} = 0.65$ to $S_{max} = 0.80$, while the lower load level remained constant at $S_{min} = 0.05$.

In order to perform a fatigue life assessment based on the S–N curves, the number of cycles to failure for different upper load levels S_{max}, measured in fatigue tests at frequencies of 2 Hz, 8.5 Hz and 55 Hz, is summarized in Fig. 4a. Linear regressions were determined for all investigated loading frequencies. However, the corresponding coefficients of determination (R^2) indicate that the quality of the regression strongly depends on the available experimental dataset. In particular, no statistically reliable regression line could be established for the loading frequency of 55 Hz due to the insufficient number of conducted fatigue tests, resulting in a low R^2 value of 0.329. Consequently, no consistent agreement with the S–N curve proposed by the fib Model Code 2010 can be observed. The fib Model Code 2010 proposes an empirical approximation of S–N curves for the normal- and high strength concrete by defining the number of cycles to failure in the range $\log\ N \leq 8$ as

$$\log\ N_f = \frac{8}{Y-1}\,(S_{max} - 1) \tag{2}$$

where the influence of the lower load level is introduced as

$$Y = \frac{0.45 + 1.8\ S_{min}}{1 + 1.8\ S_{min} - 0.3\ (S_{min})^2}. \tag{3}$$

While the assessment based on the S–N curves exhibits significant scatter, the Sparks–Menzies relation can be used to precisely evaluate compressive fatigue life. Therefore, the secondary strain rate was determined for each test and subsequently plotted on a double logarithmic scale against the number of cycles to failure, as depicted in Fig. 4b. The results obtained at 2 Hz and 8.5 Hz each exhibit a strong linear correlation as reflected by R^2 values of 0.998 and 0.989, which enables a reliable evaluation of the fatigue life. Despite the difference in loading frequency, it can also be observed that both regression lines show a similar linear trend. In contrast, no equivalent result could be obtained for the 55 Hz tests, which is partly due to the limited number of available experiments. More importantly, at loading frequencies as high as 55 Hz, the fatigue behavior is significantly affected by factors such as heat generation, which can complicate an accurate fatigue life assessment based on the Sparks–Menzies relation. Nevertheless, when considering the results across all investigated frequencies, a clear trend emerges, indicating that a higher loading frequency results in lower secondary strain rates.

To extend the analysis of compressive fatigue and further validate the Sparks–Menzies relation under different influencing parameters, an additional test series with varied concrete classes, which is part of the study presented in [17,54], was re-evaluated.

2.2. Compressive cylinder tests for varied concrete classes

The concrete used in this test series can be classified into strength classes C40, C80 and C120. The investigated concrete classes comprised C40, C80, and C120, produced using CEM II 42.5 N cement (C40) and CEM I 52.5 R cement (C80 and C120), with water-to-cement ratios of 0.50, 0.47, and 0.35, respectively. Limestone–quartz aggregates with a maximum grain size of 8 mm were used for C40, whereas C80

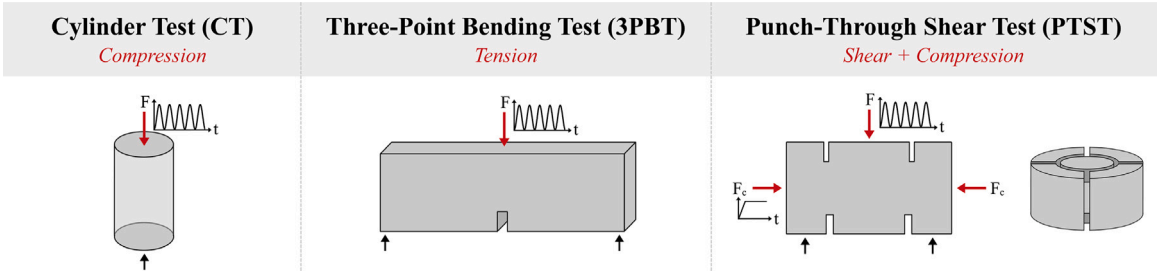


Fig. 2. Overview of the investigated fatigue test setups, including compressive, tensile, and shear configurations, used to evaluate the applicability of the Sparks–Menzies relation across different loading conditions.

contained a 50/50 limestone–quartz blend and C120 consisted entirely of quartz aggregate, both with a maximum grain size of 16 mm. The fatigue tests were performed on cylindrical specimens with diameters ranging from 100 to 150 mm and a constant height of 300 mm. As in the previous test series, the strains of the concrete cylinders were continuously measured using three LVDTs. The experiments were carried out with constant amplitudes and a loading frequency of 5 Hz. The upper load levels varied between $S_{max} = 0.65$ to $S_{max} = 0.80$, while the lower load level was set to either $S_{min} = 0.05$ or $S_{min} = 0.20$.

The established S–N curves for each investigated concrete class are shown in Fig. 4c. It can be observed that the obtained C80 regression line exhibits the best alignment with the approximated S–N curve based on Eq. (2). Notably, no reasonable linear regression could be extracted for concrete grade C120 due to the substantial scatter and insufficient number of tests, thereby highlighting limitations of fatigue life assessments based solely on the S–N curves. This underlines the necessity of a more robust analysis based on the Sparks–Menzies relation.

Therefore, the logarithmic secondary strain rate versus the logarithmic number of cycles to failure is plotted in Fig. 4d for each test in order to establish the Sparks–Menzies relation. It can be observed from the experimental results that the data points for each concrete class align very well with their respective regression lines. Furthermore, a clear trend is evident, demonstrating a decrease in secondary strain rate with increasing compressive strength, as high-strength concrete exhibits less plastic deformation, leading to a slower strain rise in the second fatigue phase. Within the experimental series on the C120 concrete, one test was intentionally stopped after approximately 5.6 million loading cycles due to the extremely long testing duration and the absence of clear indications of imminent fatigue failure. Nevertheless, the monitored strain development had already entered the secondary fatigue phase, thereby allowing the determination of the corresponding secondary strain rate, as illustrated in Fig. 5a. Based on the established Sparks–Menzies relation for the investigated C120 concrete, the corresponding fatigue life was estimated to be approximately 15.8 million cycles, as shown in Fig. 5b. Although experimental verification of this prediction was not feasible within the scope of the present study, this example highlights the potential of the Sparks–Menzies relation as a promising approach for estimating the remaining fatigue life of runout specimens. Further long-term experimental investigations are required to systematically validate this capability.

2.3. Compressive cylinder tests under varied fatigue loading sequences

The previous test series focused on compressive fatigue under constant-amplitude loading with varied parameters. Before extending the analysis to fundamentally different loading configurations, it is essential to assess whether the Sparks–Menzies relation can also be applied to compressive fatigue under variable loading sequences. Thus, in a subsequent experimental campaign, identical C40 cylinders were utilized to examine the load sequence effect. The fatigue loading was applied with a frequency of 5 Hz at two distinct levels in varying sequences: high–low (H–L) and low–high (L–H). In the higher loading range (H), the upper load level was initially set to $S_{max} = 0.75$, before being reduced to $S_{max} = 0.65$ within the lower loading range (L). The lower load level remained constant at $S_{min} = 0.05$. In the loading scenarios (H–L) and (L–H), the first load level was applied for a predetermined number of cycles, followed by continuous application of the second load level until fatigue failure.

The S–N curves provide a well established approach to evaluate the fatigue life of concrete subjected to variable amplitude loading. Fig. 6a illustrates how a simplified S–N curve can be used to determine the theoretical number of cycles to failure at constant amplitudes N_i^t for each applied load level in a (H–L) scenario. The consumed fatigue life within a loading range (H) or (L) is determined from the quotient of the applied number of loading cycles and N_i^t as

$$\eta_i = \frac{N_i}{N_i^t}. \tag{4}$$

Based on the Palmgren–Miner (P–M) rule, the overall fatigue life can be predicted through linear accumulation of the consumed fatigue life in each loading range. Thus, the fatigue failure is assumed to occur when the following condition is met:

$$\sum_{i=1}^{n} \eta_i = \sum_{i=1}^{n} \frac{N_i}{N_i^t} = 1. \tag{5}$$

However, the P–M rule was neither designed for inhomogeneous materials such as concrete, nor does it take the widely investigated load sequence effect into account [54–61]. Thus, the applicability of the linear accumulation approach is considered questionable.

Despite the pronounced scatter observed in experimental campaigns, the investigation of the load sequence effect still relies on the traditional S–N curves. Therefore, this paper introduces an alternative approach to assess the compressive fatigue behavior of concrete under variable amplitude loading, using the Sparks–Menzies relation. Fig. 6b illustrates a simplified fatigue creep curve for the (H–L) loading scenario. It can be observed that the strain rate $\Delta\varepsilon_{II,H}^{max}/\Delta N$ is determined within the second phase of the higher loading range (H), and $\Delta\varepsilon_{II,L}^{max}/\Delta N$ within the second phase of the lower loading range (L). These secondary strain rates can be used to precisely evaluate the theoretical fatigue life at constant amplitudes corresponding to each applied load level. For this purpose, a variable-amplitude test series must always be based on a constant-amplitude series using the same concrete matrix. Accordingly, an established Sparks–Menzies Eq. (1) can be rearranged to

$$N_i^t = 10^{\left(\log \varepsilon'_{II,i} - m\right)/s} \tag{6}$$

in order to obtain the theoretical numbers of cycles to failure at constant amplitudes, using secondary strain rates as an alternative to an S–N curve.

The assessment of the compressive cylinder tests with varied loading sequences was conducted based on both the S–N curve and Sparks–Menzies relation, as established for C40 concrete in Section 2.2, enabling a qualitative comparison of the evaluation approaches. The

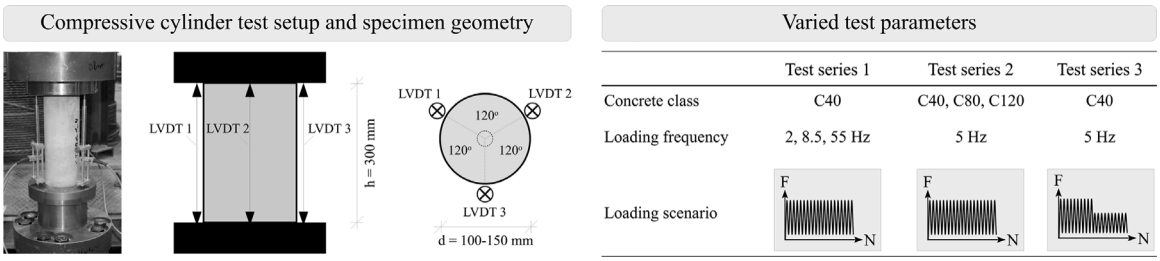


Fig. 3. Test setup and specimen geometry used in compressive cylinder tests with varied loading frequencies, concrete classes and loading sequences.

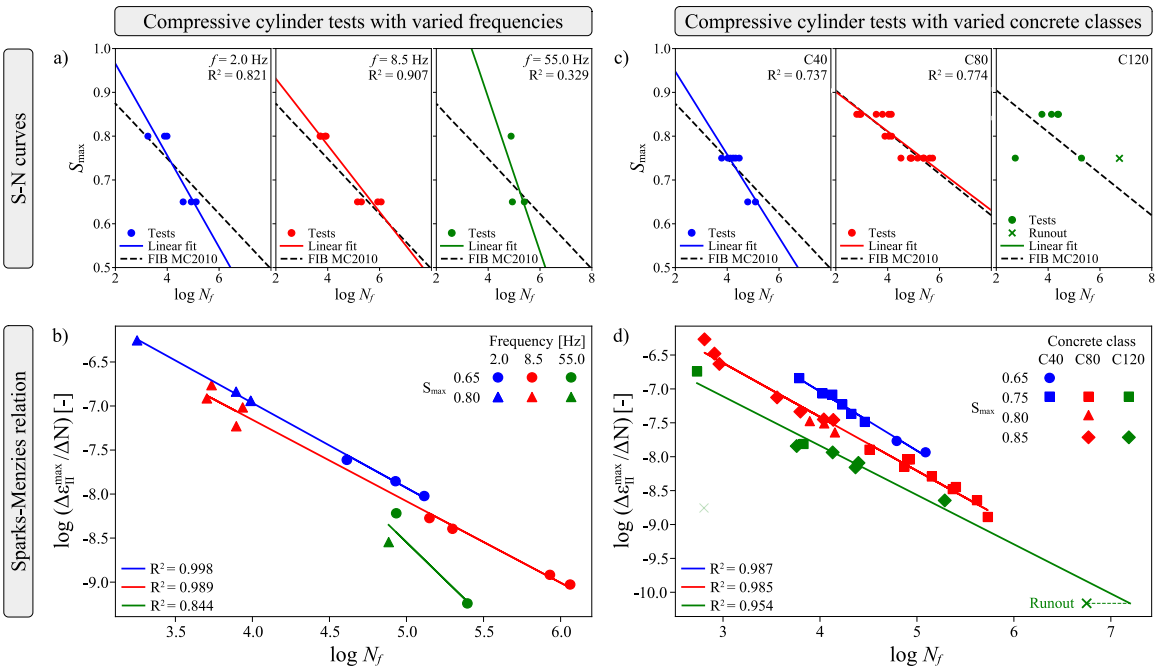


Fig. 4. Evaluation of compressive fatigue life using cylinder tests with varied loading frequencies and concrete classes: (a) S–N curves for the tests with loading frequencies of 2 Hz, 8.5 Hz and 55 Hz; (b) Sparks–Menzies relation shown with regression lines for each loading frequency; (c) S–N curves for concrete C40, C80 and C120 (d) Sparks–Menzies relation shown with regression lines for each concrete class.

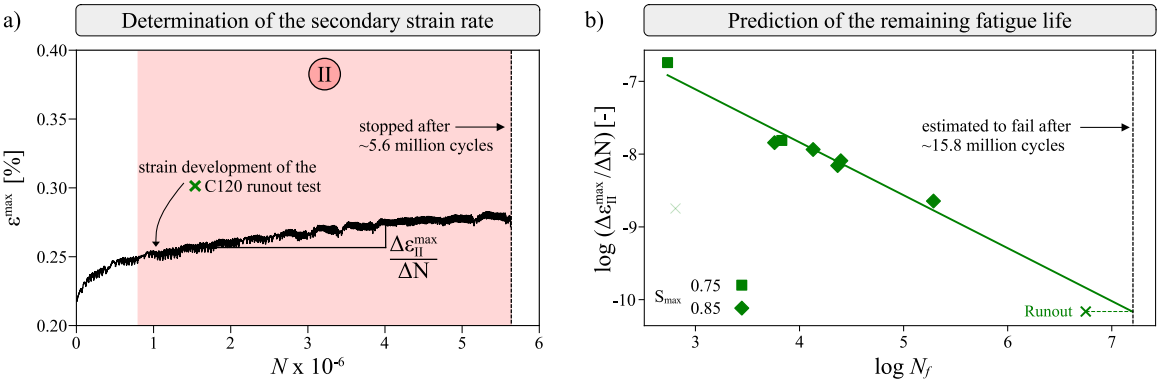


Fig. 5. Predicting the remaining fatigue life of runouts based on the Sparks–Menzies relation: (a) Secondary strain rate determined from the measured strain development of the C120 runout specimen; (b) Estimation of the number of cycles to failure using the established C120 Sparks–Menzies relation.

experimental results for all fatigue tests with (H–L) or (L–H) loading scenarios are plotted in terms of consumed fatigue life diagrams and compared with the prediction of the P–M rule in Fig. 6c and d, corresponding to evaluations based on the established S–N curve and Sparks–Menzies relation, respectively. It can be observed that based on both evaluation approaches the average of the consumed fatigue life sum $\sum \eta$ is less than 1.0 for the (H–L) sequence, indicating an unsafe prediction of the Palmgren–Miner rule. An identical trend emerges for the evaluation of the (L–H) tests based on the Sparks–Menzies relation. In contrast, using the S–N curve to determine the theoretical fatigue life at constant amplitudes for the (L–H) sequence resulted in an average value of the consumed fatigue life sum exceeding 1.0. This implies a conservative fatigue life prediction of the P–M rule for the (L–H) scenario, a finding that is further substantiated by various

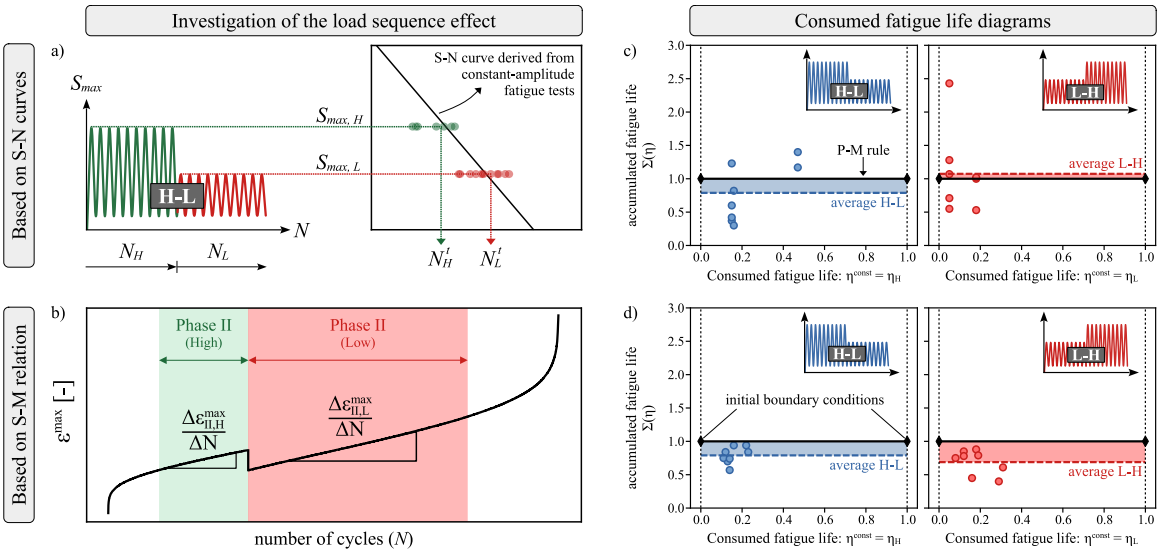


Fig. 6. Comparative investigation of the load sequence effect using both the S–N curves and the Sparks–Menzies (S–M) relation: (a) Determination of the theoretical number of cycles to failure at constant amplitudes based on the S–N curves; (b) Determining the secondary strain rates in a (H–L) loading scenario for the theoretical fatigue life estimation according to Eq. (6); c, (d) Experimental results of the fatigue tests with (H–L) and (L–H) loading scenarios summarized in consumed fatigue life diagrams based on S–N curves and Sparks–Menzies relation respectively.

studies [62–64]. Thus, both evaluation methods yield contradictory results for the (L–H) tests, whereas the strain-based assessment using the Sparks–Menzies relation exhibited significantly less scatter.

A possible explanation for this contradiction is that the strain-based assessment inherently reflects the accumulated damage state generated during the initial high-load phase. In the (L–H) scenario, the secondary strain rate measured during the subsequent lower load level is already influenced by the preceding damage accumulation, resulting in an elevated deformation growth rate and consequently a reduced predicted remaining fatigue life compared to an undamaged specimen subjected only to the lower load level. In contrast, the evaluation based on the S–N curves relies on fatigue lives obtained from constant-amplitude tests on initially undamaged specimens and therefore does not explicitly account for the influence of prior damage on the subsequent deformation evolution. Consequently, the Sparks–Menzies relation may provide a more damage-sensitive assessment of fatigue life consumption under variable loading histories. However, in order to definitively validate the observed trends, additional tests would have been needed. Within this study, only eight tests each for the (H–L) and (L–H) scenarios could be considered from the original test series [54], since several tests did not reach the secondary fatigue phase within both loading ranges (H) and (L), as required based on Fig. 6b. Consequently, the determination of two secondary strain rates was not possible, thereby preventing a fatigue life evaluation based on the Sparks–Menzies relation.

The proposed approach provides a novel framework for reliably evaluating the load sequence effect based on the Sparks–Menzies relation. However, further and more extensive experimental campaigns, specifically designed for this evaluation approach, are required in future work to obtain comprehensive results.

2.4. Three-point bending tests with varied specimen sizes

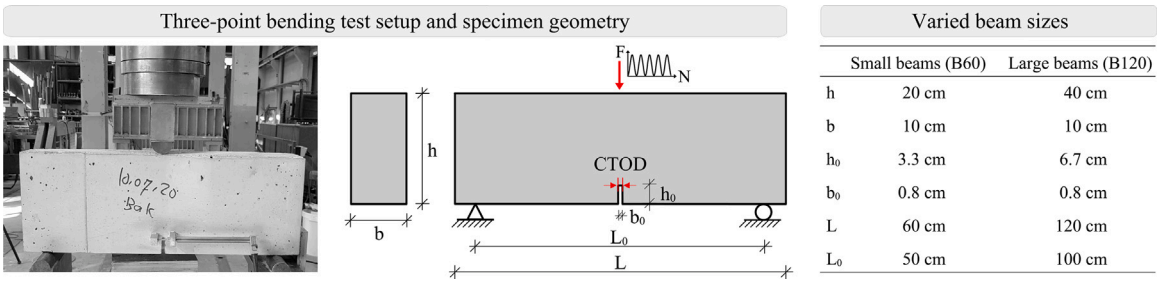
For the conditions examined so far, the Sparks–Menzies relation was found to be significantly more reliable for evaluating compressive fatigue life compared to conventional S–N curves, thereby confirming findings of previous studies [25–30]. However, a comprehensive validation of the Sparks–Menzies relation requires extending the analysis to additional loading conditions and test configurations beyond compressive cylinder tests. Therefore, this investigation re-evaluates three-point bending tests, which are part of the studies presented in [65], to further assess the applicability of the Sparks–Menzies relation under tensile fatigue loading.

The three-point bending tests were conducted on notched beams made of C60 concrete (Fig. 7). The concrete was produced using CEM I 42.5 R cement with a water-to-cement ratio of 0.39 and quartz aggregate with a maximum grain size of 8 mm. Moreover, beam specimens of two different sizes were fabricated for the tensile fatigue tests. The larger beams had a cross-sectional height of 0.4 m and a length of 1.2 m, while the smaller beams were half as high and half as long. The beam width was kept constant at 100 mm. Throughout the experiments the crack tip opening displacement (CTOD) was continuously monitored using two LVDTs, which were attached at the top of the notch in both sides of the beam. The fatigue tests were conducted with constant amplitudes and a loading frequency of 5 Hz. The upper load levels ranged from $S_{max} = 0.70$ to $S_{max} = 0.85$, while the lower load level was set to $S_{min} = 0.05$.

The S–N diagrams for fatigue tests conducted with small and large beams are plotted in Fig. 8a. The substantial scatter observed in the results, especially for the large beams within the load level $S_{max} = 0.70$, prevented a reliable assessment of fatigue life using the S–N curves. While the regression analysis for the small beams resulted in a R^2 value of 0.535, the experimental data obtained for the large beams did not allow for the derivation of a statistically reasonable regression line. In order to obtain a more reliable evaluation based on the S–N diagram, additional tests would have been needed. The results are therefore consistent with those observed in the compressive cylinder tests and once again emphasize the need for a reliable fatigue life assessment based on the Sparks–Menzies relation, here extended to tensile fatigue.

It should be noted that, unlike the compressive cylinder tests, the deformation quantity considered here is the crack tip opening displacement (CTOD), which is a fracture-related parameter influenced by the stress gradient, fracture process zone, and material toughness of the notched specimen. Consequently, the present study does not interpret CTOD as an equivalent strain measure. Instead, CTOD is adopted as the most representative deformation quantity governing fatigue crack propagation in the notched beams, allowing the underlying concept of the Sparks–Menzies relation to be examined for a fracture-dominated loading configuration.

Thus, the slope of the measured CTOD development during the second fatigue phase was determined for each test and plotted on a double



Varied beam sizes

	Small beams (B60)	Large beams (B120)
h	20 cm	40 cm
b	10 cm	10 cm
h_0	3.3 cm	6.7 cm
b_0	0.8 cm	0.8 cm
L	60 cm	120 cm
L_0	50 cm	100 cm

Fig. 7. Test setup and specimen geometry used in three-point bending tests with varied beam sizes.

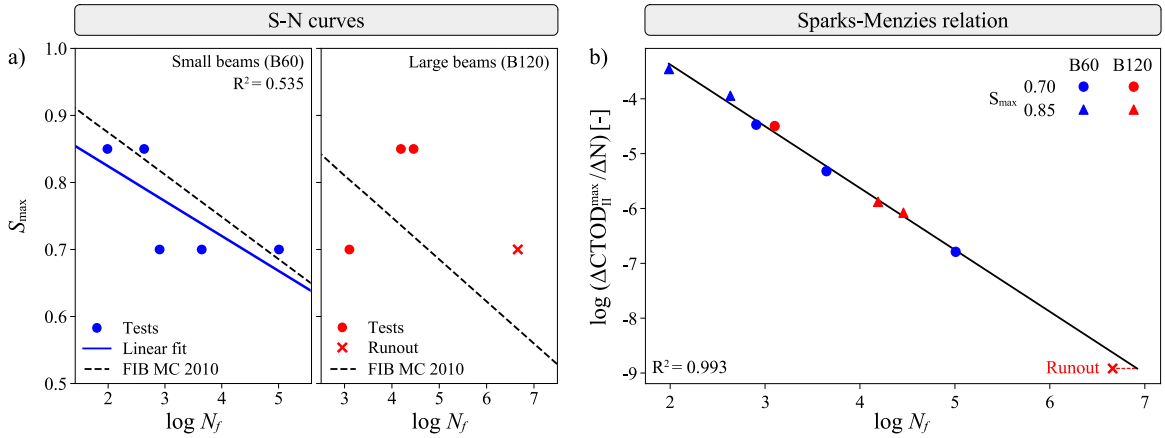


Fig. 8. Evaluation of tensile fatigue life using three-point bending tests: (a) S–N curves for small and large beams; (b) Sparks–Menzies relation shown with a combined regression line for small and large beams.

logarithmic scale with respect to the number of cycles to failure, as depicted in Fig. 8b. Despite the different beam sizes, it can be observed that all data points follow the same linear alignment, as underlined by the corresponding R^2 value of 0.993. This finding provides further evidence that there is no size effect in the Sparks–Menzies relation, as previously observed by Ortega et al. [33]. Moreover, the obtained results are remarkably consistent, indicating extremely low scatter, which enables an accurate assessment of tensile fatigue life based on the Sparks–Menzies relation. The experimental series on the large beams included a runout specimen, as one test was intentionally stopped after around 4.5 million loading cycles due to the long testing duration and the absence of clear indications of imminent failure. As already demonstrated in Section 2.2 and illustrated in Fig. 5, the Sparks–Menzies relation could be used to estimate the remaining fatigue life of such runout specimens. In this instance, the fatigue life was estimated to be approximately 8.3 million cycles. However, experimental verification of this estimation was not feasible within the scope of the present study and therefore requires further long-term experimental investigation.

2.5. Punch-through shear tests with varied lateral confinements

Having established the validity of the Sparks–Menzies relation for compressive and tensile fatigue across the majority of investigated conditions, the analysis is now extended to shear fatigue life using punch-through shear tests which are part of the studies presented in [66]. The concrete used in the multi-axial fatigue tests can be classified into strength class C80. The concrete mixture consisted of CEM I 52.5 R cement with a water-to-cement ratio of 0.35, natural sand (0–2 mm) as fine aggregate, and basalt aggregate with particle sizes ranging from 2 to 8 mm. As illustrated in the bottom-left corner of Fig. 9, the cylindrical specimens were notched to create predefined crack surfaces. The shear displacement u was determined as the average of six linear variable displacement transducers (LVDTs) mounted on the top and bottom surfaces of the specimen in order to account for possible tilting of the inner concrete core. The positions of the LVDTs together with the evaluated shear displacement u are illustrated in Fig. 9.

The constant-amplitude fatigue loading was applied with a frequency of 5 Hz. The upper load levels ranged from $S_{max} = 0.80$ to $S_{max} = 0.95$, while the lower load level remained constant at $S_{min} = 0.05$. The applied lateral compressive stress $\sigma_{c,mean}$ varied between 15 and 60 MPa. The lateral compressive stress was applied by four hydraulic cylinders, as illustrated in Fig. 9, operating under constant oil pressure to maintain an approximately constant confinement throughout the fatigue tests. The effective confinement stress was calculated as $\sigma_{c,app} = 0.9\,(4F_{cyl}/A_{Liga})$, where the factor 0.9 accounts for the non-uniform circumferential stress distribution induced by the loading configuration. A detailed description of the confinement system and the derivation of the effective confinement stress can be found in [67].

The established S–N curve for the punch-through shear tests with different lateral compressive stresses $\sigma_{c,mean}$ is plotted in Fig. 10a. The illustrated regression line exceeds the fatigue life prediction based on the fib Model Code 2010. The combined presentation of the results for all investigated levels of $\sigma_{c,mean}$ within a single S–N diagram reveals pronounced scatter, which complicates a reliable fatigue life assessment based on the S–N curve. However, with increasing σ_c, a significant decrease in scatter can be observed. Furthermore, there appears to be no correlation between the fatigue life and σ_c.

Regarding the Sparks–Menzies relation, the secondary displacement rate – here defined as the slope of the measured crack-surface displacement during the second fatigue phase, playing the same role as the secondary strain rate in compressive and tensile tests – was determined for each test and subsequently plotted on a double logarithmic scale against the number of cycles to failure, as depicted in Fig. 10b. It can be observed that all the data points align very well with a single regression line, regardless of the variations in testing parameters. Thus, the Sparks–Menzies relation is also independent of $\sigma_{c,mean}$ and can

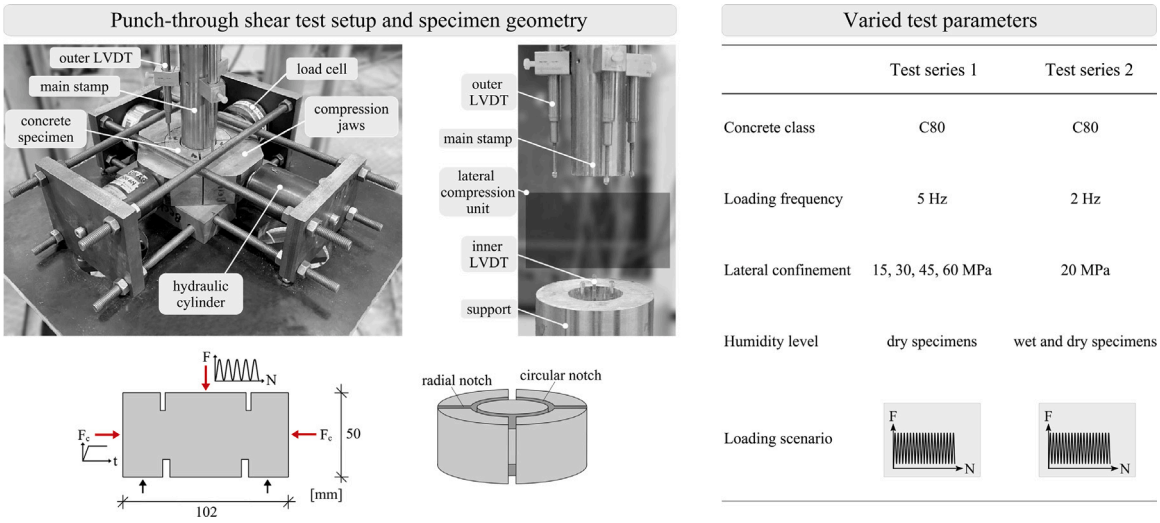


Fig. 9. Test setup and specimen geometry used in punch-through shear tests with varied lateral confinements and humidity levels.

be used to precisely evaluate the fatigue life under a combination of shear and compressive loading. Notably, the Sparks–Menzies regression yields $R^2 = 0.989$, compared with $R^2 = 0.576$ for the corresponding S–N regression, illustrating the improvement in predictive precision.

2.6. Punch-through shear tests with varied humidity

In a subsequent series of PTSTs, the effect of material moisture was investigated. The multi-axial fatigue tests were conducted on concrete of the same composition as in the previous study [66]. However, one batch of specimens was stored in a water bath for two months immediately after demolding, while another batch was dried at 105°C for one month prior to testing. Thus, two moisture conditions were distinguished. The fatigue loading was applied at constant amplitude and a frequency of 2 Hz. The upper load levels varied between $S_{max} = 0.75$ and $S_{max} = 0.95$, while the lower load level was set to $S_{min} = 0.05$. The lateral compressive loading remained constant at $\sigma_{c,mean} = 20$ MPa.

In Fig. 10c, the applied upper load levels S_{max} are plotted against the logarithmic number of cycles to failure measured in fatigue tests conducted on wet and dry specimens. In the S–N diagram for the dry specimens, it can be observed that two tests are classified as outliers. These tests exhibited an asymmetrical load distribution resulting from a significant misalignment of the testing surface. Consequently, the unintentional stress concentration on one side of the crack surface led to a substantial reduction in fatigue life. However, even beyond these outliers, the obtained results show a pronounced scatter, especially for the tests conducted on dry specimens with the load level $S_{max} = 0.75$. Meanwhile, the scatter appears to decrease due to the presence of material moisture, as can be observed in the S–N diagram for the PTSTs performed on wet specimens.

In order to provide a more reliable fatigue life evaluation based on the Sparks–Menzies relation, the logarithmic secondary displacement rate is plotted in Fig. 10d with respect to the logarithmic number of cycles to failure for each test. It can be observed that the data points for each humidity level closely follow their respective regression lines. However, the slight scatter between the evaluated wet and dry fatigue tests prevents the establishment of a completely reliable joint regression. Thus, the independence between the Sparks–Menzies relation and material moisture is not definitively proven. The results indicate that the presence of moisture in concrete is associated with a decrease in secondary strain rates. Notably, both tests identified as outliers, due to the misalignment of the testing surface, follow the same linear alignment observed for all dry fatigue tests. Thus, while the reduced fatigue life resulting from an asymmetrical load distribution may induce substantial scatter within the stress-based S–N diagram, the fatigue life evaluation based on the Sparks–Menzies relation remains unaffected by the experimental error, as the unintentionally caused reduction in fatigue life simultaneously leads to higher displacement rates within the second fatigue phase.

Overall, the conducted experimental investigations demonstrate that the Sparks–Menzies relation provides a reliable and consistent framework for evaluating fatigue life under compressive, tensile and shear loading conditions. Compared to conventional S–N curves, assessments based on the stable deformation growth within the second fatigue phase significantly reduce scatter and enable a systematic assessment of the influence of key parameters such as loading frequency, compressive strength, specimen size and humidity level.

The obtained regression constants m and s based on Eq. (1) as well as the coefficients of determination R^2 are listed in Table 1 for each test series separately.

It should be noted that the determination of the secondary strain rate was not based on a strictly fixed interval of the fatigue life. Instead, the evaluated range was selected individually for each fatigue creep curve in order to capture the actual secondary fatigue phase characterized by approximately linear deformation growth. In particular, for high stress levels S_{max}, the apparent stabilization phase often becomes significantly shorter, with the initial transient phase extending beyond 20% of the fatigue life and the onset of tertiary fatigue behavior occurring before 80%. Consequently, the evaluation interval was adapted depending on the evolution of the individual fatigue creep response in order to ensure that the measured slope corresponds to the intrinsic deformation growth rate of the secondary fatigue phase. This procedure was applied consistently to both the experimental and numerical simulation results presented in this study. The commonly adopted 20%–80% range therefore served only as a qualitative guideline consistent with existing literature [52,68]. Nevertheless, the current procedure still relies on manual identification of the secondary fatigue phase. Future work should therefore focus on automated approaches, such as the direct determination of the minimum derivative of smoothed fatigue creep curves, in order to establish a more objective and reproducible evaluation methodology.

It should be emphasized that the regression parameters m and s are not expected to represent universal material constants. Instead, they reflect the specific deformation quantity employed (strain, CTOD, or shear displacement), the governing fatigue damage mechanism, and the corresponding stress configuration. Consequently, variations

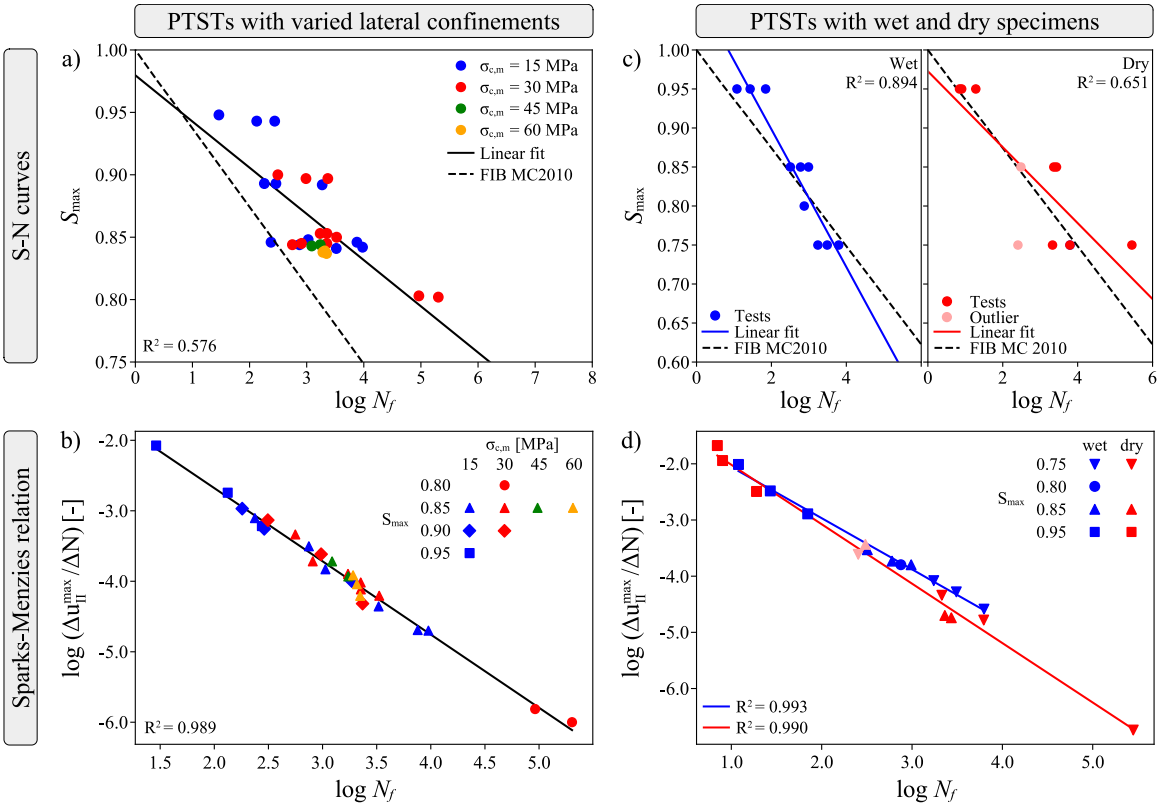


Fig. 10. Evaluation of multi-axial fatigue life using punch-through shear tests: (a) S–N curves for the tests with varied lateral confinements; (b) Sparks–Menzies relation shown with a combined regression line for the tests with varied lateral confinements; (c) S–N curves for the tests with wet and dry specimens (d) Sparks–Menzies relation shown with regression lines for the wet and dry tests.

Table 1
Regression parameters and coefficients of determination obtained from the evaluation of the Sparks–Menzies relation and the corresponding S–N curves for the investigated experimental configurations.

Test configuration	Varied parameter	Sparks–Menzies regression			S–N regression
		m	*s*	R^2	R^2
Cylinder test	f = 2 Hz	−3.106	−0.965	0.998	0.821
	f = 8.5 Hz	−3.454	−0.925	0.989	0.907
	f = 55 Hz	−0.023	−1.705	0.844	0.329
	C40	−3.546	−0.873	0.987	0.737
	C80	−4.234	−0.795	0.985	0.774
	C120	−4.929	−0.727	0.954	–
Three-point bending test	B60	−1.121	−1.127	0.993	0.535
	B120				–
Punch-through shear test	$\sigma_{c,m}$	−0.600	−1.039	0.989	0.576
	Wet	−1.147	−0.911	0.993	0.894
	Dry	−0.957	−1.058	0.990	0.651

Note: Values marked with "–" indicate cases where no meaningful linear S–N regression could be established due to the huge scatter and insufficient data.

in the regression parameters between compression, tension, and shear loading are physically expected. Nevertheless, it is noteworthy that the regression slope s remains close to −1 for most of the investigated datasets, suggesting a common inverse relationship between the logarithmic deformation rate during the secondary fatigue phase and the logarithmic fatigue life across different loading configurations. Likewise, changes in concrete strength primarily affect the magnitude of the secondary deformation rate through altered stiffness and inelastic deformation capacity, leading to shifts in the regression parameters. Establishing quantitative relationships between these parameters and intrinsic material properties requires dedicated future investigations beyond the scope of the present study.

3. Numerical analysis of concrete fatigue

To complement the experimental investigations and gain deeper insight into the mechanisms governing fatigue damage in concrete, numerical simulations are conducted using microplane and lattice discrete particle models. These mesoscale approaches allow for a direct representation of the material's heterogeneous nature and the progressive degradation processes occurring under cyclic loading. Within this framework, the experimentally validated fatigue constitutive hypothesis is formulated as an inter-aggregate constitutive model, allowing for a mechanistic interpretation of fatigue damage initiation and evolution at the mesoscale. A particular motivation of this numerical analysis is

to explore whether such models can reproduce key fatigue phenomena observed experimentally and to evaluate their potential in linking microscopic damage mechanisms with macroscopic fatigue response. In this way, the simulations aim to provide a mechanistic foundation for interpreting the Sparks–Menzies relation and to assess the feasibility of extending this strain-based concept toward a physically grounded prediction of fatigue life.

In the present study, the numerical investigations are limited to uniaxial compressive fatigue loading in order to establish the mechanistic origin of the Sparks–Menzies relation within the most extensively investigated stress configuration of concrete fatigue. Although the underlying constitutive framework is formulated in a general mixed-mode setting, the numerical assessment of the Sparks–Menzies relation under tensile and shear fatigue loading remains outside the scope of the present work and should be addressed in future studies.

3.1. Inter-aggregate fatigue constitutive framework

In order to model concrete fatigue, the authors have developed a thermodynamically based constitutive framework, which is presented in detail in [69–71]. By making use of this framework, the authors have been able to derive the formulation of an interface model that can be embedded on a generic microplane within a microplane model or at the level of inter-aggregate contact on a lattice discrete particle model. This framework is based on the hypothesis positing that fatigue damage evolution in concrete is primarily related to inter-aggregate cumulative inelastic shear strain. This hypothesis has proven valuable in modeling the fatigue behavior of cementitious interfaces and concrete under compressive fatigue loading in cylinders [48,72–74].

The relative displacement of two points connected via the interface is represented by a normal (out-of-plane) component $u_{\mathrm{N}} \equiv u_z$ and an (in-plane) sliding vector $\boldsymbol{u}_{\mathrm{T}} = \{u_x, u_y\}^{\mathsf{T}}$. The vector of kinematic variables defining the irreversible state of the interface is introduced as follows

$$\boldsymbol{\mathcal{E}} := \left[u_{\mathrm{N}}^{\mathrm{p}},\ \omega_{\mathrm{N}}, \boldsymbol{u}_{\mathrm{T}}^{\mathrm{p}},\ \omega_{\mathrm{T}},\ z_{\mathrm{T}},\ \boldsymbol{\alpha}_{\mathrm{T}}\right]. \tag{7}$$

To provide a transparent representation of dissipative mechanisms in the normal and tangential directions, the free energy is introduced as a sum of out-of-plane opening (N) and in-plane sliding (T) contributions

$$\rho\psi(\boldsymbol{\mathcal{E}}) := \rho\psi_{\mathrm{N}}(\boldsymbol{\mathcal{E}}) + \rho\psi_{\mathrm{T}}(\boldsymbol{\mathcal{E}}). \tag{8}$$

Free energy associated with interface opening and closing (N) is defined as a function of total displacement u_{N}, plastic displacement $u_{\mathrm{N}}^{\mathrm{p}}$, and damage ω_{N} as

$$\rho\psi_{\mathrm{N}}(u_{\mathrm{N}}, u_{\mathrm{N}}^{\mathrm{p}}, \omega_{\mathrm{N}}) := \frac{1}{2}\left(1 - H(\sigma_{\mathrm{N}})\,\omega_{\mathrm{N}}\right) E_{\mathrm{N}}(u_{\mathrm{N}} - u_{\mathrm{N}}^{\mathrm{p}})^2, \tag{9}$$

where E_{N} denotes the stiffness. The Heaviside step function $H(\cdot)$ is used to introduce the unilateral effect by activating the damage only for positive values of the traction stress σ_{N}.

The free energy associated with the interface sliding is defined as a function of total sliding vector $\boldsymbol{u}_{\mathrm{T}}$, plastic sliding vector $\boldsymbol{u}_{\mathrm{T}}^{\mathrm{p}}$, tangential damage ω_{T}, and the displacement variables corresponding to isotropic and kinematic hardening, z_{T} and $\boldsymbol{\alpha}_{\mathrm{T}} = [\alpha_x, \alpha_y]$, respectively, as

$$\rho\psi_{\mathrm{T}}(\boldsymbol{u}_{\mathrm{T}}, \boldsymbol{u}_{\mathrm{T}}^{\mathrm{p}}, \omega_{\mathrm{T}}, z_{\mathrm{T}}, \boldsymbol{\alpha}_{\mathrm{T}}) := \frac{1}{2}(1-\omega_{\mathrm{T}})E_{\mathrm{T}}\left[(\boldsymbol{u}_{\mathrm{T}} - \boldsymbol{u}_{\mathrm{T}}^{\mathrm{p}})^{\mathsf{T}} \cdot (\boldsymbol{u}_{\mathrm{T}} - \boldsymbol{u}_{\mathrm{T}}^{\mathrm{p}})\right] + \frac{1}{2}K_{\mathrm{T}} z_{\mathrm{T}}^2 + \frac{1}{2}\gamma_{\mathrm{T}}(\boldsymbol{\alpha}_{\mathrm{T}}^{\mathsf{T}} \cdot \boldsymbol{\alpha}_{\mathrm{T}}), \tag{10}$$

where E_{T} denotes the tangential stiffness, K_{T} the isotropic and γ_{T} the kinematic hardening moduli. The thermodynamic forces are obtained by differentiating the free energy with respect to the kinematic state variables

$$\boldsymbol{\mathcal{S}} = \boldsymbol{Y}\,\frac{\partial\rho\psi(\boldsymbol{\mathcal{E}})}{\partial\boldsymbol{\mathcal{E}}}. \tag{11}$$

The sign vector operator $\boldsymbol{Y}$ is introduced to render positive thermodynamic force for positive state variable. Following the definition of the state vector in Eq. (7), we introduce the generalized vector of thermodynamic forces as

$$\boldsymbol{\mathcal{S}} := \left[\sigma_{\mathrm{N}}^{\mathrm{p}},\ Y_{\mathrm{N}},\ \boldsymbol{\sigma}_{\mathrm{T}}^{\mathrm{p}},\ Y_{\mathrm{T}},\ Z_{\mathrm{T}},\ \boldsymbol{X}_{\mathrm{T}}\right]. \tag{12}$$

The individual components of this vector can be obtained using Eq. (11) The individual components of this vector are obtained using Eq. (11). The normal plastic stress $\sigma_{\mathrm{N}}^{\mathrm{p}}$ and normal energy release rate Y_{N} read

$$\sigma_{\mathrm{N}}^{\mathrm{p}} = -\rho\frac{\partial\psi(\boldsymbol{\mathcal{E}})}{\partial u_{\mathrm{N}}^{\mathrm{p}}} = \left(1 - H(\sigma_{\mathrm{N}}^{\mathrm{p}})\,\omega_{\mathrm{N}}\right) E_{\mathrm{N}}(u_{\mathrm{N}} - u_{\mathrm{N}}^{\mathrm{p}}), \tag{13}$$

$$Y_{\mathrm{N}} = -\rho\frac{\partial\psi(\boldsymbol{\mathcal{E}})}{\partial\omega_{\mathrm{N}}} = \frac{1}{2}E_{\mathrm{N}}(u_{\mathrm{N}} - u_{\mathrm{N}}^{\mathrm{p}})^2. \tag{14}$$

As discussed above, the Heaviside switches off the damage in compression to represent the stiffness recovery upon interface closure. The tangential plastic stress vector $\boldsymbol{\sigma}_{\mathrm{T}}^{\mathrm{p}}$, energy release rate Y_{T}, isotropic hardening stress Z_{T} and back stress $\boldsymbol{X}_{\mathrm{T}} = \{X_x, X_y\}^{\mathsf{T}}$ are obtained as follows

$$\boldsymbol{\sigma}_{\mathrm{T}}^{\mathrm{p}} = -\rho\frac{\partial\psi(\boldsymbol{\mathcal{E}})}{\partial\boldsymbol{u}_{\mathrm{T}}^{\mathrm{p}}} = (1-\omega_{\mathrm{T}})E_{\mathrm{T}}(\boldsymbol{u}_{\mathrm{T}} - \boldsymbol{u}_{\mathrm{T}}^{\mathrm{p}}) \tag{15}$$

$$Y_{\mathrm{T}} = -\rho\frac{\partial\psi(\boldsymbol{\mathcal{E}})}{\partial\omega_{\mathrm{T}}} = \frac{1}{2}E_{\mathrm{T}}\left[(\boldsymbol{u}_{\mathrm{T}} - \boldsymbol{u}_{\mathrm{T}}^{\mathrm{p}})^{\mathsf{T}} \cdot (\boldsymbol{u}_{\mathrm{T}} - \boldsymbol{u}_{\mathrm{T}}^{\mathrm{p}})\right] \tag{16}$$

$$Z_{\mathrm{T}} = \rho\frac{\partial\psi(\boldsymbol{\mathcal{E}})}{\partial z_{\mathrm{T}}} = K_{\mathrm{T}} z_{\mathrm{T}}, \quad \boldsymbol{X}_{\mathrm{T}} = \rho\frac{\partial\psi(\boldsymbol{\mathcal{E}})}{\partial\boldsymbol{\alpha}_{\mathrm{T}}} = \gamma_{\mathrm{T}}\,\boldsymbol{\alpha}_{\mathrm{T}}. \tag{17}$$

The summarized inter-aggregate constitutive model (Fig. 11a) describes the 3D interface behavior under monotonic, cyclic, and fatigue loading across all mixed-mode stress states. Compared to existing approaches, the proposed model offers key advantages: (i) damage evolution is coupled with the cumulative plastic sliding measure through potentials-based evolution laws; (ii) a convex and smooth threshold surface (Fig. 11a) defined in effective stress space ensures robust time integration with automatic handling of unloading and reloading; and (iii) the non-associative flow potential allows scalable coupling between normal and tangential damage mechanisms.

To realistically capture fatigue-induced degradation at the interface level, it is essential to employ a constitutive formulation capable of describing progressive damage accumulation under cyclic loading. Conventional damage models typically trigger damage evolution only when the slip or displacement exceeds its previous maximum value, limiting their ability to represent progressive degradation under repeated loading. To overcome this limitation and enable the realistic capture of fatigue-induced deterioration, the present fatigue damage model introduces the cumulative plastic slip as the driving measure of damage evolution. This approach allows damage to evolve continuously during both loading and unloading stages, reflecting the gradual accumulation of microcracks and interface degradation characteristic of fatigue behavior.

Fig. 11b compares the shear stress–slip responses under monotonic and cyclic loading, including two cyclic cases with different amplitudes. The results reveal that higher loading amplitudes lead to faster stiffness degradation and larger hysteresis loops. The corresponding damage evolution in Fig. 11c further demonstrates amplitude-dependent fatigue damage accumulation throughout the loading–unloading cycles, confirming the model's capability to capture fatigue-driven bond deterioration.

3.2. Implementation of the constitutive framework at different modeling scales

The inter-aggregate fatigue constitutive framework described in Section 3.1 was implemented within two independent modeling approaches in order to investigate the applicability of the proposed fatigue hypothesis at different observation scales. The first approach employs the constitutive relations within a homogenized macroscale

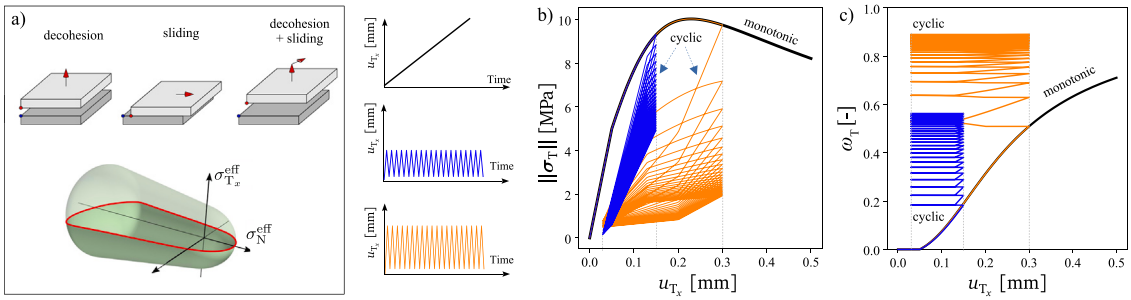


Fig. 11. (a) Illustration of the inter-aggregate fatigue constitutive model showing the kinematic modes and the initial smooth threshold function that defines the elastic domain in stress space; (b) shear response under monotonic and cyclic loading; (c) damage evolution under monotonic and cyclic loading.

microplane formulation, while the second introduces them directly at the level of inter-aggregate contacts within a meso-scale lattice discrete particle model (LDPM). In both cases, the constitutive hypothesis is motivated by experimental observations indicating that fatigue-induced degradation in concrete is strongly associated with progressive microcrack development and cumulative inelastic sliding within the inter-aggregate regions.

Fig. 12a illustrates experimentally observed microcrack evolution in concrete subjected to cyclic loading obtained from X-ray micro-CT investigations [75]. Based on these observations, the proposed constitutive framework was incorporated within the dissipative mechanisms of both the macroscale microplane model and the meso-scale LDPM, as schematically illustrated in Fig. 12b. This implementation strategy enables the investigation of whether the experimentally observed deformation-driven fatigue behavior and the associated Sparks–Menzies relation can be consistently reproduced across different modeling scales.

3.2.1. Macroscale microplane sliding model (MS1)

Unlike the classical constitutive models, which establish a direct relation between the strain and stress *tensors*, the microplane models introduce a constitutive relation between strain and stress *vectors* at the level of projected planes, effectively replicating the anisotropic behavior of concrete [40,76–78].

Kinematic constraint. The strain tensor is projected onto each microplane to obtain strain vectors consisting of the normal and tangential components using the so called kinematic constraint

$$\varepsilon_{\mathrm{N}} = \boldsymbol{N} : \boldsymbol{\varepsilon}, \qquad \boldsymbol{\varepsilon}_{\mathbf{T}} = \mathbf{T} : \boldsymbol{\varepsilon}, \tag{18}$$

where the scalar ε_{N} is the normal microplane strain, and $\boldsymbol{\varepsilon}_{\mathbf{T}}$ is the tangential microplane strain vector. The second order normal tensor $\boldsymbol{N}$ and the third order tangential tensor $\boldsymbol{T}$ are given as

$$\boldsymbol{N} = \boldsymbol{n} \otimes \boldsymbol{n}, \qquad \mathbf{T} = \boldsymbol{n} \cdot \mathbb{I}_{sym} - \boldsymbol{n} \otimes \boldsymbol{n} \otimes \boldsymbol{n}, \tag{19}$$

where $\boldsymbol{n}$ is the microplane normal vector and $\mathbb{I}$ is the fourth-order identity tensor.

Constitutive behavior. The constitutive behavior of the proposed microplane model is governed by the thermodynamically based constitutive laws described in Section 3.1 governing the macroscopic behavior. These constitutive laws are defined on the generic microplanes and introduce the dissipative mechanisms for the normal and tangential direction.

Homogenization. The macroscopic stress tensor can be obtained as follows

$$\boldsymbol{\sigma} = \boldsymbol{\beta} : \boldsymbol{C}^{\mathrm{e}} : \boldsymbol{\beta}^{\mathrm{T}} : (\boldsymbol{\varepsilon} - \boldsymbol{\varepsilon}^{\mathrm{p}}), \tag{20}$$

where $\boldsymbol{\beta}$ is the fourth order damage inverse/integrity tensor, $\boldsymbol{C}^{\mathrm{e}}$ is the fourth order elasticity tensor, and $\boldsymbol{\varepsilon}^{\mathrm{p}}$ is the macroscopic plastic strain tensor. According to [79] the macroscopic plastic strain tensor can be obtained by integrating microplane plastic strains as follows

$$\boldsymbol{\varepsilon}^{\mathbf{P}}_{\mathbf{ij}} = \frac{3}{2\pi}\int_{\Omega} \varepsilon_N^{\mathrm{P,mic}} n_i n_j \,\mathrm{d}\Omega + \frac{3}{2\pi}\int_{\Omega} \frac{\varepsilon_{Tr}^{\mathrm{P,mic}}}{2}(n_i\delta_{rj} + n_j\delta_{ri})\,\mathrm{d}\Omega. \tag{21}$$

The fourth order damage inverse/integrity tensor $\boldsymbol{\beta}$ can be obtained by integrating the normal and tangential microplane damage parameters as follows

$$\begin{aligned}\boldsymbol{\beta}_{ijkl} = {} & \frac{3}{2\pi}\int_{\Omega} \beta_{\mathrm{N}}\, n_i\, n_j\, n_k\, n_l \,\mathrm{d}\Omega \\ & + \frac{3}{2\pi}\int_{\Omega} \frac{\beta_{\mathrm{T}}}{4}\left(n_i\, n_k\delta_{jl} + n_i\, n_l\delta_{jk} + n_j\, n_k\delta_{il} + n_j\, n_l\delta_{ik} - 4n_i\, n_j\, n_k\, n_l\right)\,\mathrm{d}\Omega\end{aligned} \tag{22}$$

where $\beta_{\mathrm{N}}^{\mathrm{mic}} = \sqrt{1-\omega_{\mathrm{N}}^{\mathrm{mic}}}$ is the integrity parameter of the normal direction, and $\beta_{\mathrm{T}}^{\mathrm{mic}} = \sqrt{1-\omega_{\mathrm{T}}^{\mathrm{mic}}}$ is the integrity parameter of the tangential direction. For a comprehensive description of the microplane model MS1, including the detailed constitutive formulation, numerical implementation, and calibration procedure, the reader is referred to [48,73].

3.2.2. Mesoscale lattice discrete particle model (LDPM)

The lattice discrete particle model (LDPM) is employed for an explicit simulation of the mesostructure of concrete [50,80–87]. The model represents the material as a system of particles with translational and rotational degrees of freedom. Rigid particles represent larger aggregates with surrounding cement matrix; smaller aggregates are omitted, their role being merged into the constitutive laws on contacts of the larger rigid particles. The kinematics of the model are provided by rigid-body motion of the particles, which results in displacement jumps between them.

Spatial domain discretization. The material inner structure is characterized by Delaunay triangulation, which connects the center of each rigid particle, representing the aggregates, to create the lattice system. Then, a tessellation of the domain generates a network of polyhedral cells, which contain an aggregate surrounded by the cement matrix skeleton. The interaction between aggregates occurs through the facets of the polyhedral cells of adjacent particles.

Kinematics. The displacement $\boldsymbol{u}_p$ of an arbitrary point $\boldsymbol{p}$ within a rigid body can be expressed in terms of the displacements $\boldsymbol{u}_a$ of the particle governing node $\boldsymbol{a}$ and the rotations $\boldsymbol{\theta}_a$ of the rigid body a, as formulated in [50]

$$\boldsymbol{u}_p = \boldsymbol{u}_a + \boldsymbol{\theta}_a \times (\boldsymbol{p} - \boldsymbol{a})$$

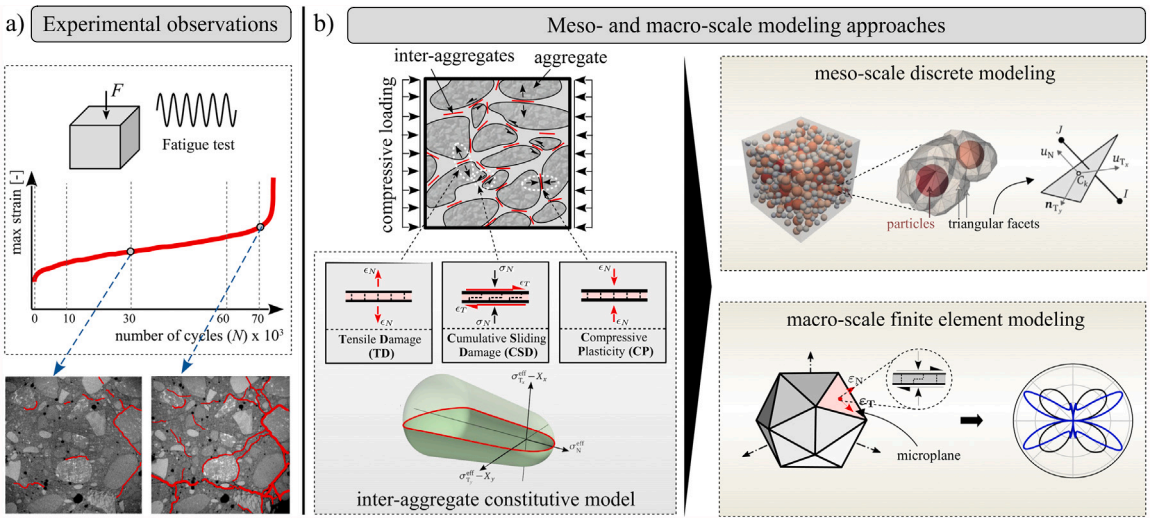


Fig. 12. (a) Experimental observations of the microcrack development within the inter-aggregate regions under fatigue loading using X-ray micro-CT images [75]; (b) Dissipative mechanisms incorporated within meso-scale lattice discrete model and macroscale microplane fatigue models [71].

$$\begin{Bmatrix} u_1^p \\ u_2^p \\ u_3^p \end{Bmatrix} = \underbrace{\begin{bmatrix} 1 & 0 & 0 & 0 & x_3^p - x_3^a & x_2^a - x_2^p \\ 0 & 1 & 0 & x_3^a - x_3^p & 0 & x_1^p - x_1^a \\ 0 & 0 & 1 & x_2^p - x_2^a & x_1^a - x_1^p & 0 \end{bmatrix}}_{\boldsymbol{A}_a^p} \begin{Bmatrix} u_1^a \\ u_2^a \\ u_3^a \\ \theta_1^a \\ \theta_2^a \\ \theta_3^a \end{Bmatrix}, \tag{23}$$

where the subscripts 1, 2, and 3 refer to the three coordinate directions. In this description of rigid body motion, small deformations and rotations are assumed. Consider two rigid bodies, a and b, with one common contact facet. Assuming arbitrary displacements and rotations for a and b, the displacement of point c at the contact facet can be expressed by substituting c and a, and c and b into Eq. (23). The difference between the displacements from both sides of each contact facet results in the following expression for the displacement jump between rigid bodies a and b at the centroid of the contact facet, $\boldsymbol{c}$.

$$\Delta \boldsymbol{u}_{ab} = \boldsymbol{A}_b^c \left[\boldsymbol{u}_b^{\mathsf{T}}, \boldsymbol{\theta}_b^{\mathsf{T}}\right]^{\mathsf{T}} - \boldsymbol{A}_a^c \left[\boldsymbol{u}_a^{\mathsf{T}}, \boldsymbol{\theta}_a^{\mathsf{T}}\right]^{\mathsf{T}}. \tag{24}$$

Stress–displacement relation. The interaction of particles is governed by constitutive relations that are applied at their contact facets. The mesoscale elastic behavior is controlled by two parameters, namely the elastic modulus in the normal direction E_{N} and in the tangential direction E_{T}. The relation between stress σ and displacements $\boldsymbol{u}$ in the elastic regime on each facet yields

$$\begin{Bmatrix} \sigma_N \\ \sigma_M \\ \sigma_L \end{Bmatrix} = \begin{bmatrix} E_{\mathrm{N}} & & \\ & E_{\mathrm{T}} & \\ & & E_{\mathrm{T}} \end{bmatrix} \begin{Bmatrix} u_N \\ u_M \\ u_L \end{Bmatrix} \tag{25}$$

In nonlinear regime, the contact constitutive behavior comes from the relations described in Section 3.1.

Balance equation. The solution of unknown displacements is obtained via enforcing the principle of virtual work. We equilibrate the work of forces (forces $\boldsymbol{f}_a$, $\boldsymbol{f}_b$ and moments $\boldsymbol{m}_a$, $\boldsymbol{m}_b$) acting on virtual nodal displacements ($\delta\boldsymbol{u}_a$, $\delta\boldsymbol{u}_b$ and $\delta\boldsymbol{\theta}_a$, $\delta\boldsymbol{\theta}_b$) with the work of forces ($\boldsymbol{s}$ from Eq. (25) multiplied by the contact area A) acting on facet virtual jumps ($\delta\boldsymbol{\Delta u}_{ab} = L\,\delta\boldsymbol{e}_{ab}$):

$$\begin{pmatrix} \boldsymbol{f}_a & \boldsymbol{m}_a & \boldsymbol{f}_b & \boldsymbol{m}_b \end{pmatrix} \begin{pmatrix} \delta\boldsymbol{u}_a & \delta\boldsymbol{\theta}_a & \delta\boldsymbol{u}_b & \delta\boldsymbol{\theta}_b \end{pmatrix}^{\mathsf{T}} = A\,\boldsymbol{\sigma}^{\mathsf{T}} \delta\boldsymbol{\Delta u}_{ab} \tag{26}$$

For a detailed presentation of the lattice discrete particle model formulation, including mesostructural discretization, constitutive implementation, and numerical solution strategy, the reader is referred to [49].

3.3. Numerical investigation of the Sparks–Menzies relation

3.3.1. Macroscale assessment using the microplane model MS1

Following the constitutive framework summarized in Section 3.2.1, the capability of the microplane model MS1 [48] to reproduce the experimentally observed Sparks–Menzies relation was first investigated at the macroscale level. The simulations represent a homogenized material-point idealization of a uniaxial compressive fatigue test on cylindrical concrete specimens, as illustrated in Fig. 13a. Cyclic loading was applied using maximum stress levels $S_{\max}$ ranging from 0.80 to 0.975, while the minimum stress level was kept constant at $S_{\min} = 0.05$. The material parameters adopted for the simulations correspond to the calibrated microplane fatigue model for C40 concrete reported in [48].

The computed fatigue creep curves are shown in Fig. 13b. For all investigated loading levels, the simulations reproduce the characteristic three-stage fatigue evolution typically observed in concrete under cyclic compression. In particular, a pronounced secondary fatigue phase associated with an approximately constant strain rate is clearly captured by the model. This behavior emerges naturally from the progressive accumulation of inelastic sliding and damage incorporated within the constitutive formulation.

To evaluate the applicability of the Sparks–Menzies relation, the strain rates corresponding to the secondary fatigue phase were extracted from the simulated creep curves and correlated with the corresponding number of cycles to failure. The resulting double-logarithmic representation is presented in Fig. 13c. The numerical results exhibit a clear linear relationship between the logarithmic secondary strain rate and the logarithmic fatigue life. All simulated data collapse onto a nearly unique straight line, demonstrating that the microplane formulation consistently reproduces the experimentally observed deformation-based fatigue characterization.

For comparison, the experimentally obtained regression line for C40 concrete is additionally included in Fig. 13c. Although the numerical simulations generally predict somewhat lower secondary strain rates for a given fatigue life, the numerical and experimental trends exhibit very similar slopes. The observed differences can be attributed to the homogenized material-point representation adopted by the microplane

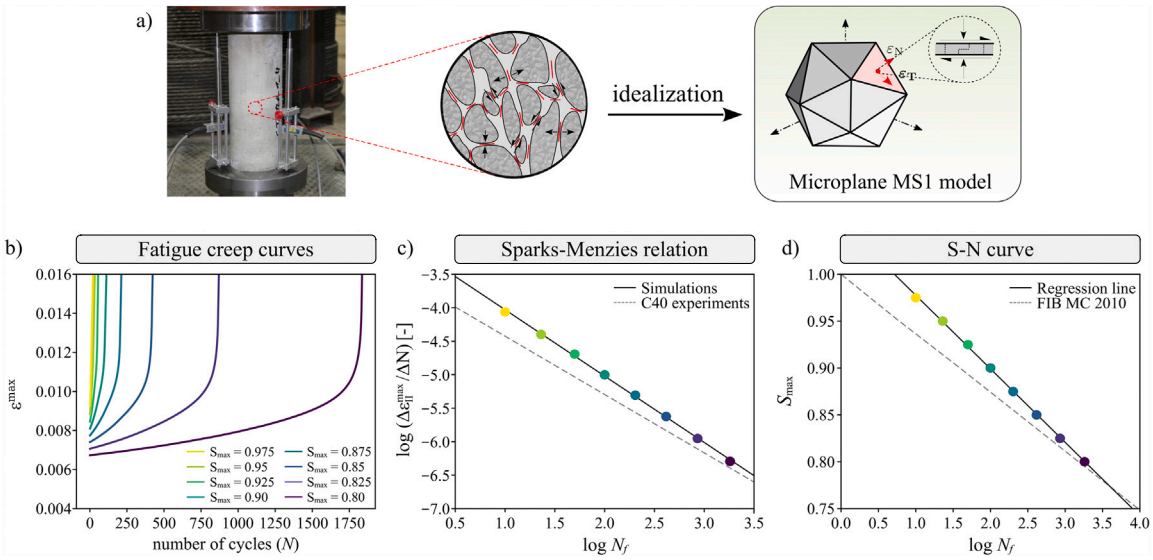


Fig. 13. Simulation of compressive fatigue behavior using microplane model MS1: (a) Single material point idealization of the cylinder test under uni-axial compression; (b) Fatigue creep curves obtained for simulations with varied upper load levels S_{max}; (c) Fatigue life evaluation based on the Sparks–Menzies relation; (d) Fatigue life evaluation based on the S–N curve.

model, which neglects explicit mesostructural heterogeneity, geometric imperfections, and localized cracking processes. Nevertheless, the overall agreement confirms that the proposed constitutive framework captures the essential mechanisms governing progressive deformation accumulation during cyclic loading.

The fatigue simulations were additionally evaluated using the classical stress-based S–N representation shown in Fig. 13d. While the model reproduces a reasonable S–N trend, the predicted fatigue lives are generally longer than those suggested by the fib Model Code 2010. More importantly, the stress-based representation alone provides limited insight into the underlying fatigue degradation process and does not exploit the stable deformation growth observed during the secondary fatigue phase. In contrast, the Sparks–Menzies relation directly links the rate of deformation accumulation to the remaining fatigue life and therefore provides a physically more informative fatigue characterization.

It should be noted that the present microplane simulations are performed at the material-point level and are therefore intended to reproduce the constitutive evolution of fatigue deformation rather than the structural failure mode of the tested cylinders. Although friction at the specimen–loading plate interfaces may induce stress non-homogeneity and influence the final crack localization observed experimentally, the secondary fatigue phase is predominantly governed by distributed damage and stable deformation accumulation, for which the homogeneous stress assumption is considered appropriate. The influence of mesostructural heterogeneity and strain localization is subsequently addressed by the lattice discrete particle model presented in Sections 3.3.2 and 3.3.3, where crack initiation and localization emerge naturally.

Overall, the macroscale simulations demonstrate that the Sparks–Menzies relation can be consistently reproduced within a homogenized constitutive framework. This finding suggests that the stable deformation growth observed during the secondary fatigue phase is not merely an empirical feature of experimental measurements, but rather an inherent consequence of the underlying fatigue degradation mechanisms incorporated within the constitutive model.

3.3.2. *Mesostructural investigation using LDPM prism simulations*

While the macroscale simulations demonstrate that the Sparks–Menzies relation can be reproduced at the constitutive level, the underlying mesostructural mechanisms governing this behavior remain unresolved. To further investigate the physical origin of the relation, fatigue simulations were conducted using the lattice discrete particle model (LDPM) developed by the authors [49]. In contrast to the homogenized microplane formulation, the LDPM explicitly represents the heterogeneous mesostructure of concrete, including aggregate interactions, crack initiation, and localized dissipation processes.

Concrete prism specimens with dimensions of 50 × 50 × 100 mm were subjected to cyclic uniaxial compression. The simulated mesostructure included aggregates with sizes ranging from 8–16 mm, enabling explicit representation of inter-aggregate interactions and localized deformation mechanisms. Fatigue loading was applied using maximum stress levels between $S_{max} = 0.80$ and 0.975, while the minimum stress level was maintained at $S_{min} = 0.05$. The constitutive and mesostructural parameters were adopted from the calibrated LDPM formulation presented in [49]. These simulations were carried out using the MARS LDPM solver [88–90].

The resulting fatigue creep curves shown in Fig. 14a reproduce the characteristic three-stage fatigue evolution observed experimentally and in the macroscale simulations. In particular, the secondary fatigue phase is again characterized by a nearly constant deformation growth rate. Based on these curves, the secondary strain rates were extracted and correlated with the corresponding number of cycles to failure, as shown in Fig. 14b.

The numerical results reveal a pronounced linear relationship between the logarithmic secondary strain rate and the logarithmic fatigue life, in agreement with the experimentally observed Sparks–Menzies relation. The agreement between experiments, macroscale constitutive simulations, and mesostructure-resolved LDPM simulations demonstrates that the relation emerges consistently across different modeling scales and therefore reflects a fundamental characteristic of fatigue degradation in concrete rather than a purely empirical correlation.

The corresponding stress-based fatigue assessment is shown in Fig. 14c together with the fib Model Code 2010 reference curve [53]. The LDPM reproduces the overall S–N trend well, particularly at intermediate and high stress levels. Nevertheless, similarly to the macroscale simulations, the stress-based representation alone does not provide direct insight into the deformation accumulation mechanisms governing fatigue deterioration.

To further elucidate the physical origin of the observed strain-rate-controlled fatigue behavior, the spatial distributions of tangential plastic dissipation and tangential damage dissipation are presented in Fig. 14d and e for representative stages corresponding to approximately

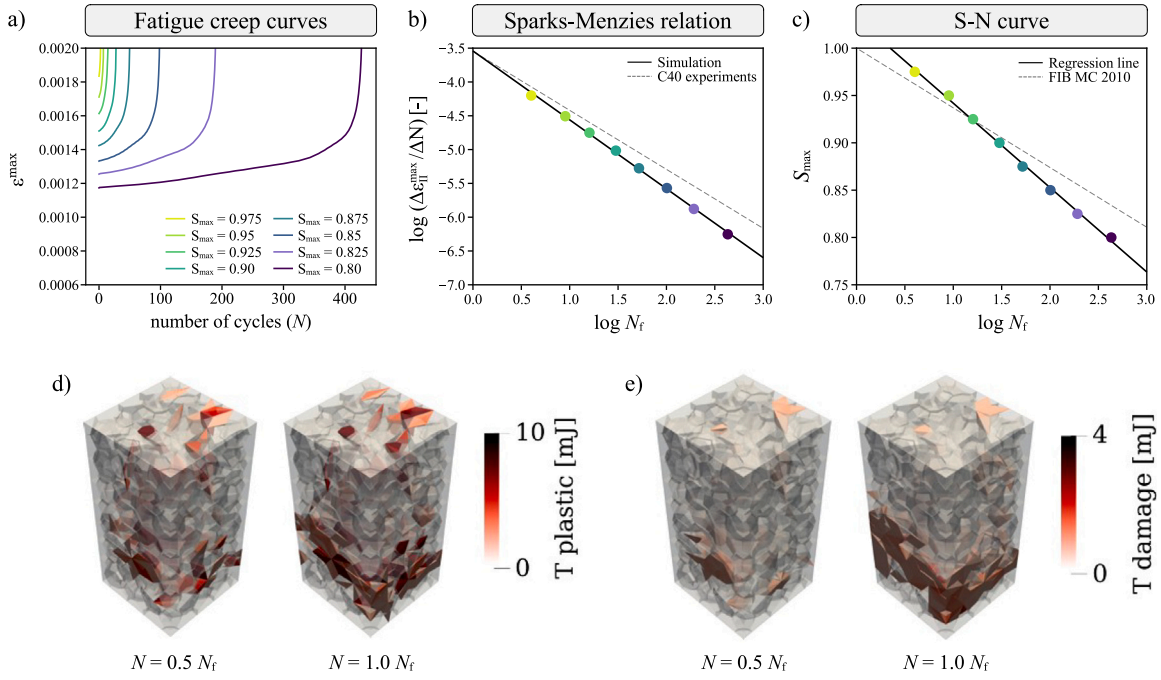


Fig. 14. Simulation of compressive fatigue behavior using lattice discrete particle model (LDPM): (a) Fatigue creep curves obtained for simulations with varied upper load levels S_{max}; (b) Fatigue life evaluation based on the Sparks–Menzies relation; (c) Fatigue life evaluation based on the S–N curve; (d) Spatial distribution of tangential plastic dissipation across lattice facets at two different stages during fatigue life; (e) Spatial distribution of tangential damage dissipation across lattice facets at two different stages during fatigue life.

50% and 100% of the fatigue life. During the secondary fatigue phase, tangential plastic dissipation is broadly distributed over a large number of lattice facets, particularly within inter-aggregate regions subjected to shear transfer. This response indicates stable accumulation of irreversible sliding processes throughout the mesostructure. As fatigue progresses, the plastic dissipation gradually localizes into continuous bands that eventually coincide with the final fracture path.

In contrast, tangential damage dissipation remains relatively limited during most of the fatigue life and becomes strongly localized only near failure, marking the transition from stable degradation to rapid stiffness loss and macroscopic fracture. This complementary evolution of plastic dissipation and damage localization provides direct mesostructural evidence that the secondary fatigue phase is primarily governed by cumulative inelastic sliding processes, whereas damage localization dominates the final failure stage. Consequently, the linear correlation underlying the Sparks–Menzies relation can be interpreted as a macroscopic manifestation of the stable accumulation of inter-aggregate inelastic dissipation during cyclic loading.

3.3.3. LDPM cylinder simulations with different specimen sizes and comparison with literature data

To further investigate the robustness and transferability of the Sparks–Menzies relation, additional mesoscale discrete simulations were performed on cylindrical concrete specimens with two different geometrical sizes [91]. The first specimen had a radius of 0.075 m and a height of 0.30 m, while the second specimen had a radius of 0.05 m and a height of 0.20 m, as illustrated in Fig. 15. In contrast to the previously investigated prism specimens, these simulations enable assessment of the relation for geometries commonly adopted in experimental fatigue investigations and facilitate direct comparison with literature data.

The mesostructure was generated using a minimum particle spacing of 8 mm. The constitutive parameters adopted for the simulations correspond to the inter-aggregate fatigue framework summarized in Section 3.2.2. The following material parameters were used: density $\rho = 2200$ kg/m^3, normal stiffness $E_N = 80$ GPa, tangential stiffness $E_T = 0.3E_N$, tensile strength $f_t = 4.1$ MPa, compressive strength $f_c = 40$ MPa, shear strength $f_s = 0.9$ MPa, kinematic hardening moduli $\gamma_N = 40$ GPa and $\gamma_T = 0.2$ GPa, damage energy scaling parameter $S_T = 0.06$ GPa, damage rate exponent $r_T = 1$, damage accumulation exponent $c_T = 1$, and pressure sensitivity parameter $p_T = 0.0012$. The parameter p_T (denoted m in [71]) is the pressure sensitivity coefficient of the smooth threshold surface; for its full expression see [71]. Boundary conditions were imposed through kinematic constraints applied to the top and bottom loading surfaces. Since the present investigation focuses primarily on pre-peak fatigue behavior, simulations were conducted using fixed rotational degrees of freedom at the upper loading surface.

The monotonic compressive responses obtained for the two cylinder sizes are shown in Fig. 15a,b. Both specimens exhibit nearly identical peak compressive strengths, indicating only limited size dependence within the investigated geometrical range. Following the monotonic calibration, cyclic loading simulations were conducted for several stress ranges while maintaining a constant lower stress level of $S_{min} = 0.05$. The investigated upper stress levels were $S_{max} = 0.70, 0.85, 0.90, 0.95$.

The computed stress–strain responses under cyclic loading reproduce the characteristic fatigue features observed experimentally, including progressive accumulation of irreversible strains, gradual stiffness degradation, and the formation of hysteretic loops. The corresponding fatigue creep curves additionally reveal the characteristic secondary fatigue phase associated with approximately constant deformation growth rates.

The obtained S–N curves for both cylinder sizes are shown in Fig. 15c. The numerical results for both specimen sizes almost overlap, indicating that the predicted fatigue behavior is only weakly influenced by specimen geometry within the investigated range.

To evaluate the applicability of the Sparks–Menzies relation, the secondary strain rates were extracted from the approximately linear portions of the fatigue creep curves between 20% and 60% of the fatigue life, as highlighted in Fig. 15d. The selected interval reflects the earlier onset of tertiary fatigue behavior observed in the numerical

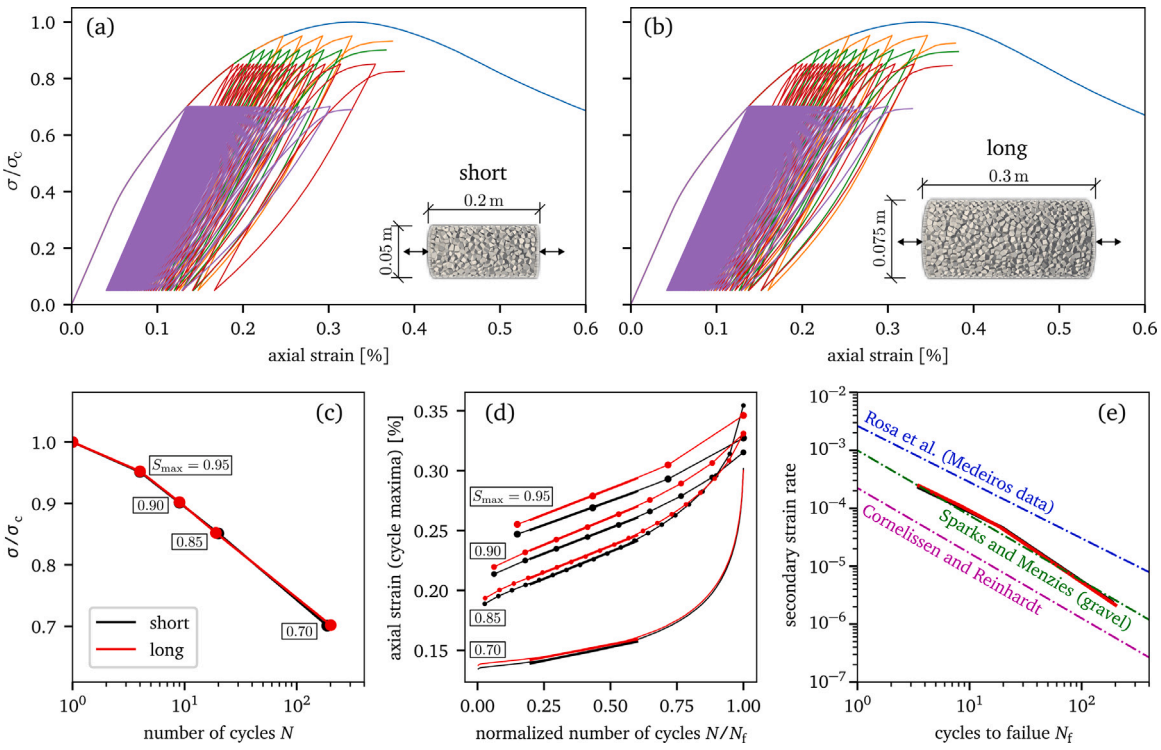


Fig. 15. Compressed cylinders (small and large). Panels: (a) and (b) stress–strain curves of monotonic and fatigue loading for cylindrical specimen under uniaxial compression; (c) S–N curve; (d) Fatigue creep curve reporting strains at upper stress level against normalized number of cycles; (e) Sparks–Menzies plot compared relating the secondary strain rate with the fatigue life.

simulations and was chosen to ensure that the evaluated slope corresponds exclusively to the approximately linear secondary fatigue phase. The resulting Sparks–Menzies plots are presented in Fig. 15e together with experimentally reported relations from Sparks and Menzies [24], Cornelissen and Reinhardt [92], and the recent Bayesian analysis by De La Rosa et al. [30].

The simulated results consistently reproduce the experimentally observed decrease of the secondary strain rate with increasing fatigue life. Moreover, the numerical data obtained for both cylinder sizes follow trends comparable to the experimentally reported power-law relationships. The close agreement across different specimen geometries, modeling scales, and literature datasets further supports the interpretation that the Sparks–Menzies relation reflects a fundamental fatigue mechanism associated with the stable accumulation of irreversible deformation during the secondary fatigue phase.

Together with the previously presented macroscale and prism-scale simulations, these additional cylinder analyses provide comprehensive multiscale numerical evidence supporting the general validity and robustness of the Sparks–Menzies relation for concrete subjected to cyclic compression.

4. Conclusions

This study systematically investigated the Sparks–Menzies relation as a strain-based alternative to conventional S–N curves for the assessment of fatigue life in concrete. A comprehensive experimental program covering compressive, tensile, and shear fatigue loading was combined with meso- and macro-scale numerical simulations in order to critically examine the hypothesis that the linear relationship between the logarithmic deformation rate in the secondary fatigue phase and the logarithmic number of cycles to failure represents a robust and physically meaningful fatigue life indicator. The main findings of the study can be summarized as follows:

- The Sparks–Menzies relation enabled a reliable assessment of compressive fatigue life across different concrete classes and loading frequencies. The experimental results consistently produced coefficients of determination between $R^2 = 0.954$ and 0.998, substantially exceeding those obtained from the corresponding S–N regressions ($R^2 = 0.329$–0.907). The secondary strain rate decreased systematically with increasing loading frequency and compressive strength.
- A novel strain-based evaluation of load sequence effects was conducted using the Sparks–Menzies relation. For the high–low (H–L) sequence, both the S–N–based and strain-based evaluations indicated reduced fatigue life compared to the Palmgren–Miner prediction. In contrast, contradictory trends were observed for the low–high (L–H) scenario, where the S–N–based evaluation yielded conservative predictions, while the Sparks–Menzies relation indicated reduced fatigue life due to elevated secondary strain rates induced by the initial high-load phase. However, the analysis was limited by the absence of a clearly identifiable secondary fatigue phase in several tests.
- Tensile fatigue behavior investigated by means of notched three-point bending tests demonstrated that the Sparks–Menzies relation can be established independently of specimen size. A nearly perfect linear correlation ($R^2 = 0.993$) between the logarithmic crack tip opening displacement rate and the logarithmic fatigue life confirmed the robustness and size-independence of the strain-based fatigue life indicator.
- The assessment of punch-through shear tests further confirmed the applicability of the Sparks–Menzies relation under shear-dominated loading. Strong linear correlations were obtained independently of the confinement level ($R^2 = 0.989$) and for both wet and dry moisture conditions ($R^2 = 0.993$ and 0.990, respectively), demonstrating the robustness of the strain-based fatigue life indicator.

- Meso- and macro-scale numerical simulations provided independent confirmation of the Sparks–Menzies relation and offered mechanistic insight into its physical origin. Both the microplane constitutive model and the lattice discrete particle model reproduced the characteristic three-stage fatigue behavior and the stable rate of deformation growth in the secondary fatigue phase, demonstrating that the observed linear relation emerges naturally from physically motivated fatigue degradation mechanisms associated with cumulative inelastic sliding and damage evolution.

Taken together, the presented experimental and numerical results demonstrate that the Sparks–Menzies relation constitutes a robust and physically meaningful strain-based fatigue life indicator for concrete across different loading configurations, specimen geometries, and modeling scales. Compared to conventional S–N–based approaches, the proposed framework exhibits significantly reduced scatter while additionally enabling the estimation of the remaining fatigue life of runout specimens. Future research should focus on extending the proposed framework to variable-amplitude loading conditions, clarifying the influence of environmental effects, and further linking microscale fatigue degradation mechanisms with monitoring-based lifetime prediction approaches for concrete structures.

CRediT authorship contribution statement

Wassim Kerkeni: Writing – original draft, Visualization, Validation, Methodology, Investigation, Formal analysis. **Abedulgader Baktheer:** Writing – original draft, Visualization, Validation, Methodology, Funding acquisition, Data curation, Conceptualization. **Mario Aguilar:** Methodology, Investigation, Data curation. **Henrik Becks:** Investigation. **Miroslav Vořechovský:** Writing – review & editing, Visualization, Methodology, Investigation, Funding acquisition, Data curation. **Martin Classen:** Supervision, Funding acquisition. **Rostislav Chudoba:** Writing – review & editing, Supervision, Funding acquisition, Conceptualization.

Declaration of Generative AI and AI-assisted technologies in the writing process

During the preparation of this work, the author(s) used ChatGPT (OpenAI) to assist in improving the clarity and conciseness of the language. After using this tool, the author(s) carefully reviewed and edited the content as needed and take full responsibility for the final content of the publication.

Declaration of competing interest

The authors declare that they have no known competing financial interests or personal relationships that could have appeared to influence the work reported in this paper.

Acknowledgments

The work of Wassim Kerkeni, Abedulgader Baktheer, Henrik Becks, and Martin Classen was supported by the German Research Foundation (DFG) within the project “Deciphering the effect of load sequence in concrete fatigue: An interleaved numerical–experimental methodology” (Project No. 544805481).

The work of Mario Aguilar, Rostislav Chudoba, and Miroslav Vořechovský was supported by the European Union’s Horizon Europe Research and Innovation Programme under the European Research Council (ERC) Synergy Grant Agreement No. 101167045 (FatResCon). This support is gratefully acknowledged.

Data availability

Data will be made available on request.

References

[1] Miarka P, Seitl S, Bílek V, Cifuentes H. Assessment of fatigue resistance of concrete: S-N curves to the Paris’ law curves. Constr Build Mater 2022;341:127811. http://dx.doi.org/10.1016/j.conbuildmat.2022.127811.

[2] Becks H, Aguilar M, Baktheer A, Chudoba R, Claßen M. Experimental and numerical investigations on the fatigue behavior of high-strength concrete under combined shear-compression loading. In: IABSE symposium prague 2022: Challenges for existing and oncoming structures. Prague, Czech Republic; 2022, p. 532–40. http://dx.doi.org/10.2749/prague.2022.0532.

[3] Oneschkow N, Timmermann T, Löhnert S. Compressive fatigue behaviour of high-strength concrete and mortar: Experimental investigations and computational modelling. Materials 2022;15(1). http://dx.doi.org/10.3390/ma15010319.

[4] Engelhardt M, Kalytta-Mewes A, Volkmer D, Lohmann J, Ritter M, Schaan G, Schmidt-Döhl F, Ali MA, Basaldella M, Haist M, Kern B, Lohaus L, Oneschkow N, Rozanski C, Timmermann T, Grosse CU, Birtel V, Garrecht H, Madadi H, Markert M, Steeb H. Micro- and nanostructural investigations of high and ultra-high performance concrete under fatigue. Int J Fatigue 2025;199:109038. http://dx.doi.org/10.1016/j.ijfatigue.2025.109038.

[5] Baktheer A, Aldakheel F. Physics-based machine learning for fatigue lifetime prediction under non-uniform loading scenarios. Comput Methods Appl Mech Engrg 2025;444:118116. http://dx.doi.org/10.1016/j.cma.2025.118116.

[6] Aguilar M, Baktheer A, Chudoba R. On the energy dissipation in confined concrete subjected to shear cyclic loading. Proc Appl Math Mech 2023;22(1):e202200301. http://dx.doi.org/10.1002/pamm.202200301.

[7] Becks H, Baktheer A, Marx S, Classen M, Hegger J, Chudoba R. Monitoring concept for the propagation of compressive fatigue in externally prestressed concrete beams using digital image correlation and fiber optic sensors. Fatigue Fract Eng Mater Struct 2023;46(2):514–26. http://dx.doi.org/10.1111/ffe.13881.

[8] Seemab F, Schmidt M, Baktheer A, Classen M, Chudoba R. Automated detection of propagating cracks in RC beams without shear reinforcement based on DIC-controlled modeling of damage localization. Eng Struct 2023;286:116118. http://dx.doi.org/10.1016/j.engstruct.2023.116118.

[9] Becks H, Lippold L, Winkler P, Moeller M, Rohrer M, Leusmann T, Anton D, Sprenger B, Kähler P, Rudenko I, Andrés Arcones D, Koutsourelakis P-S, Unger JF, Weiser M, Petryna Y, Schnellenbach-Held M, Lowke D, Wessels H, Lenzen A, Zabel V, Könke C, Claßen M, Hegger J. Neuartige Konzepte für die Zustandsüberwachung und -analyse von Brückenbauwerken – Einblicke in das Forschungsvorhaben SPP100+. Bauingenieur 2024;99(10):327–38. http://dx.doi.org/10.37544/0005-6650-2024-10-63.

[10] Herbers M, Richter B, Gebauer D, Classen M, Marx S. Crack monitoring on concrete structures: Comparison of various distributed fiber optic sensors with digital image correlation method. Struct Concr 2023;24(5):6123–40. http://dx.doi.org/10.1002/suco.202300062.

[11] Antonaci P, Bocca P, Masera D. Fatigue crack propagation monitoring by acoustic emission signal analysis. Eng Fract Mech 2012;81:26–32. http://dx.doi.org/10.1016/j.engfracmech.2011.09.017, Fracture and Damage Analysis in Design.

[12] Noorsuhada MN. An overview on fatigue damage assessment of reinforced concrete structures with the aid of acoustic emission technique. Constr Build Mater 2016;112:424–39. http://dx.doi.org/10.1016/j.conbuildmat.2016.02.206.

[13] Do M-T, Chaallal O, Aïtcin P-C. Fatigue behavior of high-performance concrete. J Mater Civ Eng 1993;5(1):96–111. http://dx.doi.org/10.1061/(ASCE)0899-1561(1993)5:1(96).

[14] Schneider S. Frequenzabhängigkeit des ermüdungswiderstandes von hochfestem beton (Ph.D. thesis), Hannover: Gottfried Wilhelm Leibniz Universität Hannover; 2021, http://dx.doi.org/10.15488/11147.

[15] Tomann C, Oneschkow N. Influence of moisture content in the microstructure on the fatigue deterioration of high-strength concrete. Struct Concr 2019;20(4):1204–11. http://dx.doi.org/10.1002/suco.201900023.

[16] Baktheer A, Spartali H, Chudoba R, Hegger J. Concrete splitting and tip-bearing effect in the bond of anchored bars tested under fatigue loading in the push-in mode: An experimental investigation. Mater Struct 2022;55(3):101. http://dx.doi.org/10.1617/s11527-022-01935-7.

[17] Baktheer ARA, Camps BH, Hegger J, Chudoba R. Numerical and experimental investigations of concrete fatigue behavior exposed to varying loading ranges. In: Bulletin / international federation for structural concrete. Vol. 87, Lausanne: International Federation for Structural Concrete; 2018, p. 1083–96, Presented at the 5th International fib Congress, Melbourne, Australia.

[18] Miarka P, Ríos JD, Malíková L, Bílek V. Fatigue resistance of concrete revisited: Wide range data from low-cycle to high-cycle and influence of aggregate on fatigue lifetimes. Cem Concr Compos 2026;166:106394. http://dx.doi.org/10.1016/j.cemconcomp.2025.106394.

[19] Kim J-K, Kim Y-Y. Experimental study of the fatigue behavior of high strength concrete. Cem Concr Res 1996;26(10):1513–23. http://dx.doi.org/10.1016/0008-8846(96)00151-2.

[20] Oneschkow N. Fatigue behaviour of high-strength concrete with respect to strain and stiffness. Int J Fatigue 2016;87:38–49. http://dx.doi.org/10.1016/j.ijfatigue.2016.01.008.

[21] Xiong Z, Liu X, Li J, Baktheer A, Wolters K, Feldmann M. An accelerated phase-field model for high-cycle fatigue behaviour in quasi-brittle materials. Theor Appl Fract Mech 2025;105003. http://dx.doi.org/10.1016/j.tafmec.2025.105003.

[22] Claßen M, Gallwoszus J. Concrete fatigue in composite dowels. Struct Concr 2016;17(1):63–73. http://dx.doi.org/10.1002/suco.201400120.

[23] Liu F, Zhou J. Research on fatigue strain and fatigue modulus of concrete. Adv Civ Eng 2017;2017(1):6272906. http://dx.doi.org/10.1155/2017/6272906.

[24] Sparks PR, Menzies JB. The effect of rate of loading upon the static and fatigue strengths of plain concrete in compression. Mag Concr Res 1973;25(83):73–80. http://dx.doi.org/10.1680/macr.1973.25.83.73.

[25] Cachim PB, Figueiras JA, Pereira PAA. Fatigue behavior of fiber-reinforced concrete in compression. Cem Concr Compos 2002;24(2):211–7. http://dx.doi.org/10.1016/S0958-9465(01)00019-1.

[26] Isojeh B, El-Zeghayar M, Vecchio FJ. Concrete damage under fatigue loading in uniaxial compression. ACI Mater J 2017;114(2):225–35. http://dx.doi.org/10.14359/51689477.

[27] Hümme J, von der Haar C, Lohaus L, Marx S. Fatigue behaviour of a normal-strength concrete – number of cycles to failure and strain development. Struct Concr 2016;17(4):637–45. http://dx.doi.org/10.1002/suco.201500139.

[28] Oneschkow N. Analyse des ermüdungsverhaltens von beton anhand der dehnungsentwicklung. Hannover: Leibniz Universität Hannover. Institut für Baustoffe; 2014, http://dx.doi.org/10.15488/357.

[29] Ali MA, Oneschkow N, Lohaus L, Haist M. Influence of the load frequency and moisture content on fatigue deterioration of high-strength concrete. Ce/Papers 2023;6(6):849–55. http://dx.doi.org/10.1002/cepa.2837.

[30] De La Rosa Á, Yu RC, Ruiz G. Fatigue life prediction in cementitious materials through Bayesian probabilistic models. Fatigue Fract Eng Mater Struct 2025;48(8):3434–64. http://dx.doi.org/10.1111/ffe.14678.

[31] You F, Luo S, Zheng J, Wang G, Wang Y. Effect of the loading frequency on the compressive fatigue behavior of recycled aggregate concrete. Constr Build Mater 2026;524:146294. http://dx.doi.org/10.1016/j.conbuildmat.2026.146294.

[32] Poveda E, Ruiz G, Cifuentes H, Yu RC, Zhang X. Influence of the fiber content on the compressive low-cycle fatigue behavior of self-compacting SFRC. Int J Fatigue 2017;101:9–17. http://dx.doi.org/10.1016/j.ijfatigue.2017.04.005.

[33] Ortega JJ, Ruiz G, Poveda E, González DC, Tarifa M, Zhang XX, Yu RC, Vicente M, de La Rosa Á, Garijo L. Size effect on the compressive fatigue of fibre-reinforced concrete. Constr Build Mater 2022;322:126238. http://dx.doi.org/10.1016/j.conbuildmat.2021.126238.

[34] Schäfer N, Gudžulić V, Timothy JJ, Breitenbücher R, Meschke G. Fatigue behavior of HPC and FRC under cyclic tensile loading: Experiments and modeling. Struct Concr 2019;20(4):1265–78. http://dx.doi.org/10.1002/suco.201900056.

[35] Alrayes O, Könke C, Ooi ET, Hamdia KM. Modeling cyclic crack propagation in concrete using the scaled boundary finite element method coupled with the cumulative damage-plasticity constitutive law. Materials 2023;16(2). http://dx.doi.org/10.3390/ma16020863.

[36] Zhou R, Lu Y, Wang W, Cheng C, Lu Z. Mesoscale modelling of the dynamic tensile strength enhancement of concrete in spalling tests using interface elements. Eng Fract Mech 2024;295:109808. http://dx.doi.org/10.1016/j.engfracmech.2023.109808.

[37] Baktheer A, Martínez-Pañeda E, Aldakheel F. Phase field cohesive zone modeling for fatigue crack propagation in quasi-brittle materials. Comput Methods Appl Mech Engrg 2024;116834. http://dx.doi.org/10.1016/j.cma.2024.116834.

[38] Harper PW, Hallett SR. A fatigue degradation law for cohesive interface elements–Development and application to composite materials. Int J Fatigue 2010;32(11):1774–87. http://dx.doi.org/10.1016/j.ijfatigue.2010.04.006.

[39] Bažant ZP, Oh BH. Microplane model for fracture analysis of concrete structures. In: Proceedings of the symposium on the interaction of non-nuclear munitions with structures. 1983, p. 49–55.

[40] Kirane K, Bažant ZP. Microplane damage model for fatigue of quasibrittle materials: Sub-critical crack growth, lifetime and residual strength. Int J Fatigue 2015;70:93–105. http://dx.doi.org/10.1016/j.ijfatigue.2014.08.012.

[41] Baktheer A, Aguilar M, Chudoba R. Comprehensive review of the microplane framework for constitutive modeling focused on homogenization approaches. Arch Comput Methods Eng 2025. http://dx.doi.org/10.1007/s11831-025-10350-4.

[42] Alliche A. Damage model for fatigue loading of concrete. Int J Fatigue 2004;26(9):915–21. http://dx.doi.org/10.1016/j.ijfatigue.2004.02.006.

[43] Desmorat R, Ragueneau F, Pham H. Continuum damage mechanics for hysteresis and fatigue of quasi-brittle materials and structures. Int J Numer Anal Methods Geomech 2007;31(2):307–29. http://dx.doi.org/10.1002/nag.532.

[44] Kindrachuk VM, Thiele M, Unger JF. Constitutive modeling of creep-fatigue interaction for normal strength concrete under compression. Int J Fatigue 2015;78:81–94. http://dx.doi.org/10.1016/j.ijfatigue.2015.03.026.

[45] Lemaitre J, Desmorat R. Engineering damage mechanics: Ductile, creep, fatigue and brittle failures. Berlin, Heidelberg: Springer; 2005, p. 380. http://dx.doi.org/10.1007/b138882.

[46] Baktheer A, Chudoba R. Classification and evaluation of phenomenological numerical models for concrete fatigue behavior under compression. Constr Build Mater 2019;221:661–77. http://dx.doi.org/10.1016/j.conbuildmat.2019.06.022.

[47] Baktheer A, Goralski C, Hegger J, Chudoba R. Stress configuration-based classification of current research on fatigue of reinforced and prestressed concrete. Struct Concr 2024. http://dx.doi.org/10.1002/suco.202300667.

[48] Baktheer A, Aguilar M, Chudoba R. Microplane fatigue model MS1 for plain concrete under compression with damage evolution driven by cumulative inelastic shear strain. Int J Plast 2021;143. http://dx.doi.org/10.1016/j.ijplas.2021.102950.

[49] Aguilar M, Vořechovský M, Baktheer A, Chudoba R. Concrete fatigue propagation from material to structure: Multiscale validation of a thermodynamically based discrete model on prisms and prestressed beams. Eng Fract Mech 2026;111931. http://dx.doi.org/10.1016/j.engfracmech.2026.111931.

[50] Cusatis G, Pelessone D, Mencarelli A. Lattice discrete particle model (LDPM) for failure behavior of concrete. I: Theory. Cem Concr Compos 2011;33(9):881–90. http://dx.doi.org/10.1016/j.cemconcomp.2011.02.011.

[51] Rybczynski S, Schaan G, Dosta M, Ritter M, Schmidt-Döhl F. Discrete element modeling and electron microscopy investigation of fatigue-induced microstructural changes in ultra-high-performance concrete. Materials 2021;14(21). http://dx.doi.org/10.3390/ma14216337.

[52] Baktheer A, Chudoba R. Experimental study of the interacting effects of loading rate and temperature on concrete fatigue behavior under compression. Constr Build Mater 2025;458:139466. http://dx.doi.org/10.1016/j.conbuildmat.2024.139466.

[53] Fédération internationale du béton. Fib model code for concrete structures 2010. Berlin, Germany: Ernst & Sohn; 2013.

[54] Baktheer A, Chudoba R. Experimental and theoretical evidence for the load sequence effect in the compressive fatigue behavior of concrete. Mater Struct 2021;54(2):82. http://dx.doi.org/10.1617/s11527-021-01667-0.

[55] Becks H, Classen M. New insights into the load sequence effect: Experimental characterization and incremental modeling of plain high-strength concrete under mode II fatigue loading with variable amplitude. Int J Fatigue 2024;185:108334. http://dx.doi.org/10.1016/j.ijfatigue.2024.108334.

[56] Holmen JO. Fatigue of concrete by constant and variable amplitude loading. ACI J Spec Publ 1982;75:71–110. http://dx.doi.org/10.14359/6402.

[57] Hoff A, Høiseth K, Hanerstad TA. Testing of high strength lightweight aggregate concrete elements. Nord Concr Res 1984;(3):63–91.

[58] Hilsdorf HK, Kesler CE. Fatigue strength of concrete under varying flexural stresses. ACI J Proc 1966;63(10):1059–76. http://dx.doi.org/10.14359/7662.

[59] Tepfers R, Fridén C, Georgsson L. A study of the applicability to the fatigue of concrete of the Palmgren-Miner partial damage hypothesis. Mag Concr Res 1977;29(100):123–30. http://dx.doi.org/10.1680/macr.1977.29.100.123.

[60] Oh BH. Cumulative damage theory of concrete under variable-amplitude fatigue loadings. Mater J 1991;88(1):41–8. http://dx.doi.org/10.14359/2357.

[61] Hamdy UMA. A damage-based life prediction model of concrete under variable amplitude fatigue loading (Ph.D. thesis), The University of Iowa; 1998.

[62] Holmen JO. Fatigue of concrete by constant and variable amplitude loading. ACI J Spec Publ 1982;75:71–110. http://dx.doi.org/10.14359/6402.

[63] Petkovic G, Lenschow R, Stemland H, Rosseland S. Fatigue of high-strength concrete. Spec Publ 1990;121:505–26. http://dx.doi.org/10.14359/3740.

[64] Aguilar M, Baktheer ARA, Chudoba R. Numerical investigation of load sequence effect and energy dissipation in concrete due to compressive fatigue loading using the new microplane fatigue model MS1. In: Oñate E, Peric D, Chiumenti M, de Souza Neto E, editors. XVI international conference on computational plasticity: Fundamentals and applications. COMPLAS 2021, Barcelona, Spain: Scipedia, S.L.; 2021, p. 1–12. http://dx.doi.org/10.23967/complas.2021.053.

[65] Baktheer A, Becks H. Fracture mechanics based interpretation of the load sequence effect in the flexural fatigue behavior of concrete using digital image correlation. Constr Build Mater 2021;307. http://dx.doi.org/10.1016/j.conbuildmat.2021.124817.

[66] Becks H, Aguilar M, Chudoba R, Classen M. Characterization of high-strength concrete under monotonic and fatigue mode II loading with actively controlled level of lateral compression. Mater Struct 2022;55(10):252. http://dx.doi.org/10.1617/s11527-022-02087-4.

[67] Becks H, Aguilar M, Baktheer A, Chudoba R, Classen M. Experimental and numerical investigations on the fatigue behavior of high-strength concrete under combined shear-compression loading. In: IABSE Proceedings of IABSE symposium: Challenges for existing and oncoming structures. Prague, Czech Republic; 2022, p. 532–40.

[68] Oneschkow N. Fatigue behaviour of high-strength concrete with respect to strain and stiffness. Int J Fatigue 2016;87:38–49. http://dx.doi.org/10.1016/j.ijfatigue.2016.01.008.

[69] Baktheer A, Chudoba R. Modeling of bond fatigue in reinforced concrete based on cumulative measure of slip. In: Computational modelling of concrete structures. EURO-C 2018, CRC Press; 2018, p. 767–76. http://dx.doi.org/10.1201/9781315182964-90.

[70] Baktheer A, Chudoba R. Pressure-sensitive bond fatigue model with damage evolution driven by cumulative slip: Thermodynamic formulation and applications to steel- and FRP-concrete bond. Int J Fatigue 2018;113:277–89. http://dx.doi.org/10.1016/j.ijfatigue.2018.04.020.

[71] Chudoba R, Vořechovský M, Aguilar M, Baktheer A. Coupled sliding–decohesion–compression model for a consistent description of monotonic and fatigue behavior of material interfaces. Comput Methods Appl Mech Engrg 2022;398:115259. http://dx.doi.org/10.1016/j.cma.2022.115259.

[72] Baktheer A, Aguilar M, Hegger J, Chudoba R. Microplane damage plastic model for plain concrete subjected to compressive fatigue loading. In: Pijaudier-Cabot G, Grassl P, La Borderie C, editors. 10th international conference on fracture mechanics of concrete and concrete structures: FraMCoS-X. Bayonne, France; 2019, p. 1–12. http://dx.doi.org/10.21012/FC10.233196.

[73] Baktheer A, Esfandiari S, Aguilar M, Becks H, Classen M, Chudoba R. Fatigue-induced stress redistribution in prestressed concrete beams modeled using the constitutive hypothesis of inter-aggregate degradation. Fatigue Fract Eng Mater Struct 2024. http://dx.doi.org/10.1111/ffe.14388.

[74] Aguilar M, Baktheer A, Chudoba R. Multi-axial fatigue of high-strength concrete: Model-enabled interpretation of punch-through shear test response. Eng Fract Mech 2024;311:110532. http://dx.doi.org/10.1016/j.engfracmech.2024.110532.

[75] Skarzynski L, Marzec I, Tejchman J. Fracture evolution in concrete compressive fatigue experiments based on X-ray micro-CT images. Int J Fatigue 2019;122:256–72. http://dx.doi.org/10.1016/j.ijfatigue.2019.02.002.

[76] Caner FC, Bažant ZP. Microplane model M7 for plain concrete. I: Formulation. J Eng Mech 2012;139(12):1714–23.

[77] Caner FC, Bažant ZP. Microplane model M7 for plain concrete. II: Calibration and verification. J Eng Mech 2013;139(12):1724–35. http://dx.doi.org/10.1061/(ASCE)EM.1943-7889.0000571.

[78] Aguilar M, Baktheer A, Becks H, Classen M, Chudoba R. Fatigue-induced concrete fracture under combined compression and shear studied using standard cylinder and refined punch-through shear test setup. In: 11th international conference on fracture mechanics of concrete and concrete structures. 2023, http://dx.doi.org/10.21012/FC11.092350.

[79] Carol I, Bažant ZP. Damage and plasticity in microplane theory. Int J Solids Struct 1997;34(29):3807–35. http://dx.doi.org/10.1016/S0020-7683(96)00238-7.

[80] Cusatis G, Bažant Z, Cedolin L. Confinement-shear lattice CSL model for fracture propagation in concrete. Comput Methods Appl Mech Engrg 2006;195(52):7154–71. http://dx.doi.org/10.1016/j.cma.2005.04.019, Computational Modelling of Concrete.

[81] Bolander JE, Eliáš J, Cusatis G, Nagai K. Discrete mechanical models of concrete fracture. Eng Fract Mech 2021;257:108030. http://dx.doi.org/10.1016/j.engfracmech.2021.108030.

[82] Eliáš J, Vořechovský M, Skoček J, Bažant Z. Stochastic discrete meso-scale simulations of concrete fracture: Comparison to experimental data. Eng Fract Mech 2015;135:1–16. http://dx.doi.org/10.1016/j.engfracmech.2015.01.004.

[83] Eliáš J, Vořechovský M. Fracture in random quasibrittle media: I. Discrete meso-scale simulations of load capacity and fracture process zone. Eng Fract Mech 2020;235:107160. http://dx.doi.org/10.1016/j.engfracmech.2020.107160.

[84] Vořechovský M, Eliáš J. Fracture in random quasibrittle media: II. Analytical model based on extremes of averaging process. Eng Fract Mech 2020;235:107155. http://dx.doi.org/10.1016/j.engfracmech.2020.107155.

[85] Baktheer A, Classen M. A review of recent trends and challenges in numerical modeling of the anisotropic behavior of hardened 3D printed concrete. Addit Manuf 2024;89:104309. http://dx.doi.org/10.1016/j.addma.2024.104309.

[86] Eliáš J, Le J-L. Modeling of mode-I fatigue crack growth in quasibrittle structures under cyclic compression. Eng Fract Mech 2012;96:26–36. http://dx.doi.org/10.1016/j.engfracmech.2012.06.019.

[87] Alnaggar M, Pelessone D, Cusatis G. Lattice discrete particle modeling of reinforced concrete flexural behavior. J Struct Eng 2019;145(1):04018231. http://dx.doi.org/10.1061/(ASCE)ST.1943-541X.0002230.

[88] Cibelli A, Wan-Wendner R, Wan-Wendner L, Vorel J, Pelessone D. MARS: A multiphysics framework for the analysis of cast and printed concrete. In: Li K, Fang D, editors. 16th international conference on durability of building materials and components, proceedings. Beijing, China: CIMNE; 2023, p. 8. http://dx.doi.org/10.23967/c.dbmc.2023.050.

[89] Wang J, Vorel J, Botte W, Pelessone D, Wan-Wendner R. Adaptive lattice discrete particle model for concrete. Comput Struct 2025;317:107925. http://dx.doi.org/10.1016/j.compstruc.2025.107925.

[90] Wang J, Vorel J, Botte W, Pelessone D, Wan-Wendner R. Efficient approaches for modeling and simulating the mechanical behavior of concrete using lattice discrete particle models. Comput Struct 2024;305:107557. http://dx.doi.org/10.1016/j.compstruc.2024.107557.

[91] Vořechovský M, Sadílek V, Eliáš J, Květoň J, Mašek J. Mesoscale discrete modeling of monotonic, cyclic and fatigue loading of concrete. In: Meschke G, Pichler B, Rots JG, editors. Computational modelling of concrete and concrete structures. London: CRC Press; 2026, p. 10. http://dx.doi.org/10.1201/9781003660026-6, Proceedings of EURO-C 2026, Seefeld in Tirol, Austria, March 9–12, 2026.

[92] Cornelissen HAW, Reinhardt HW. Uniaxial tensile fatigue failure of concrete under constant-amplitude and programme loading. Mag Concr Res 1984;36(129):216–26. http://dx.doi.org/10.1680/macr.1984.36.129.216.